A Novel Squid-Inspired AUV Design: Revolutionizing Coral Reef Preservation Through CFD and Experimental Insights into Drag and Maneuverability

Zixuan Li

Abstract:

This study focuses on conceptualizing and optimizing an advanced bionic robotic solution to surmount the limitations of current observational vehicles in coral reef conservation. Human divers are traditionally subjected to physiological challenges, while current robotic alternatives grapple with operational impediments, including anthropogenic marine disturbances. Utilizing advanced robotics tailored for marine ecosystems with intricate topologies and fragile corals, this study aims to enhance conservation precision in the face of climatic shifts and marine pollution from anthropogenic activities.

This paper develops a squid-inspired Autonomous Underwater Vehicle (AUV), whose behavior is then examined and improved utilizing both experiments and Computational Fluid Dynamics.

(CFD). The governing equations considered here are the incompressible Reynolds-Averaged Navier-Stokes (RANS) with an iterative solver for both the pressure-Poisson and momentum equations. Apart from CFD analysis, a prototype was assembled and experimentally tested to validate the CFD outcomes and assess the lift from its bionic rudders. The maneuverability is optimized through careful designs and parameter studies of several features.

A head length is determined to balance viscous and pressure drag while achieving the least total drag in the AUV design. Additionally, a disk is introduced at the AUV's front, which reduces fluid contact, thereby decreasing the viscous drag. While this modification slightly increased pressure drag, it yielded an overall reduction in total drag. Experimental observations confirmed a propulsion speed and underscored the necessity for maximizing rudder extension.

The developed AUV's squid-like design, optimized via CFD, ensures drag reduction by 5.34% and energy efficiency. By mimicking squid dynamics, disturbances to marine biota are minimized. The incorporation of bionic fins, empirically fine-tuned, enhances the AUV's agility. These attributes establish it as an exceptional prototype, setting a precedent for future coral reef monitoring systems and augmenting conservation strategies.

Keywords: Computational fluid dynamics(CFD), Autonomous underwater vehicle(AUV), Coral reef preservation, Navier-Stokes equations, Hydrodynamic analysis, Biomechanics, Squid, Drag reduction

1 Introduction

Coral reefs are essential biomes that serve as home to millions of species, earning them the name "rainforests of the ocean." Approximately 25% of the ocean's fish rely on corals for shelter, food, and opportunities for reproduction in their nooks and crannies. For instance, the shallow Northwest Hawaiian Island coral reefs, a famous Papaha¯naumokua¯kea National Marine Monument sector, host over 7,000 species of fish, plants, and other living organisms [7]. On the other hand, deep-water coral reefs are less familiar to humans, yet they support a vast array of marine life in an otherwise barren world. Expanding our perspective beyond ecological concerns, coral reefs also benefit humans significantly. They protect coastlines from storms and erosion, generate employment for local communities, and provide exceptional opportunities for tourism and recreation. Additionally, coral reefs are a source of food and medicine. Globally, over half a billion people rely on coral reefs for income, protection, and sustenance. Furthermore, coral reefs contribute hundreds of millions of dollars to local economies through fishing, diving, and tourism, with an estimated net worth exceeding 10 billion US dollars [13].

Regrettably, these precious gifts are currently facing severe threats. Some of these threats are natural, such as diseases, predators, and weather events, while others are anthropogenic, including pollution, sedimentation, and climate change. These threats can result in physical damage to the ecosystems, coral bleaching, and, potentially, coral mortality. For example, Australia's once internationally renowned Great Barrier Reef has experienced extensive coral bleaching over hundreds of

miles [6]. Although recovery from bleaching is possible, it can take many years or even decades for the coral reefs to regenerate, even under favorable conditions. Numerous scientists are exploring new strategies for preserving coral reef ecosystems, necessitating a detailed understanding of coral reefs and their current conditions.
[16].
One must first comprehend them and their present circumstances to aid in preserving coral reefs. Presently, prominent organizations like the National Oceanic and Atmospheric Administration (NOAA) are engaged in long-term monitoring of the biological aspects of coral reef ecosystems. They conduct research, assessments, and restoration projects utilizing divers and large underwater robots. However, both methods have their limitations. Divers are susceptible to dangerous creatures like lionfish, encounter difficulties navigating tight and confined spaces, and experience long-term decompression sickness and related illnesses. On the other hand, existing robots are bulky and noisy, rendering them unsuitable for maneuvering through a complex ecosystem like the coral reef, with its numerous obstacles [13].
The complex coral reef environment has necessitated a surge in the demand for small autonomous underwater vehicles (AUVs) due to their promising potential for effective operation. This scientific paper proposes a bionic prototype, inspired by the remarkable characteristics of squids, to address the challenges encountered in this demanding setting. Noteworthy features of the prototype include its compact size, enabling seamless traversal of intricate biomes, emulation of squid movement mechanics through the implementation of a water pump system to mitigate seagrass threats and minimize disturbances to marine fauna, and utilization of bionic fins crafted from flexible materials to optimize maneuverability while minimizing potential harm to delicate coral structures [12].
This paper aims to investigate and enhance the hydrodynamic characteristics of the proposed bionic squid AUV, specifically focusing on the hydrodynamics forces analysis. The study initiates by optimizing the head, seeking an intricate analysis of the drag contributions from pressure and viscous effects to minimize the total drag force experienced. This research's overarching objective is to augment energy efficiency and maneuverability, central to which is the application of Computational Fluid Dynamics (CFD). CFD, an extensively employed methodology for probing flow dynamics, serves as a tool to analyze and test the pertinent variables. It also provides a vivid visual representation of the complex flow field, thus enabling a comprehensive understanding of the underlying fluid physics inherent to the robot's operation. Furthermore, this paper explores the effect of a cavity region in the head extension. It examines its potential to decrease the suction drag experienced by the robot by mitigating the pressure difference between the head and the rear of the AUV. This modification also significantly reduces fluid-wall contact, lowering the viscous drag. Through rigorous CFD analysis, accompanied by visualization of CFD-post such as wall pressure and streamlined representation, an optimal distance between the disk and the actual head is attained, highlighting the efficacy of the design enhancements.
To conduct the Computational Fluid Dynamics (CFD) analysis, the SolidWorks 3D assembly file of the bionic squid AUV was imported into the ANSYS Fluent software program. This allowed for the generation of an outer shell analysis domain, the creation of a mesh that accurately resolves fluid behavior, the execution of calculations, and the generation of visualizations about pressure, in-plane pressure, streamlines, and velocity.
To sum up, this study presents a robotic approach and optimization to the complex issue of monitoring coral reefs and their ecosystems, with the ultimate goal of preserving these invaluable species against climate change and water pollution threats. The paper is systematically organized into distinct sections. Section 2 outlines the research methods employed in the study, encompassing both computational and experimental techniques. Section 3 delves into the theoretical analysis underpinning the approach, providing a solid conceptual framework. In Section 4, the hydrodynamics based on the CFD are examined and analyzed to further optimize the drag force experienced and investigate the underlying flow physics. Furthermore, Section 5 focuses on the experimental results that validate the computational findings while exploring additional aspects of the prototype. Finally, Section 6 provides a comprehensive conclusion, summarizing the findings of this study and elucidating its potential implications.

2 Methodology

2.1 Computational Fluid Dynamics (CFD)

Originating in the early 1950s, modern CFD has become a robust numerical approximation for solving the governing equations of fluid Motion. CFD can produce numerical analogs of the fluid behavior by discretizing a set of partial differential equations. This is achieved by dividing the domain into smaller grids and considering the flow parameters and boundary conditions. The governing equations can be approximated with these inputs, resulting in a computational solution. In the context of this study, this process is specifically applied to determine the drag force experienced by the AUV [19].

2.1.1 Governing Equations

The flow past a bionic squid AUV is assumed to be isothermal and incompressible flow, and the governing equations are as follows:

$$\frac{\partial u_x}{\partial x}+\frac{\partial u_y}{\partial y}+\frac{\partial u_z}{\partial z}=0 \tag{1}$$

$$u_x\frac{\partial u_x}{\partial x}+u_y\frac{\partial u_x}{\partial y}+u_z\frac{\partial u_x}{\partial z}=-\frac{1}{\rho}\frac{\partial P}{\partial x}+_v\frac{\partial^2 u_x}{\partial x^2}+\frac{\partial^2 u_x}{\partial y^2}+\frac{\partial^2 u_x}{\partial z^2} \tag{2}$$

$$u_x\frac{\partial u_y}{\partial x}+u_y\frac{\partial u_y}{\partial y}+u_z\frac{\partial u_y}{\partial z}=-\frac{1}{\rho}\frac{\partial P}{\partial y}+_v\frac{\partial^2 u_y}{\partial x^2}+\frac{\partial^2 u_y}{\partial y^2}+\frac{\partial^2 u_y}{\partial z^2} \tag{3}$$

$$u_x\frac{\partial u_z}{\partial x}+u_y\frac{\partial u_z}{\partial x}+u_z\frac{\partial u_z}{\partial z}=-\frac{1}{\rho}\frac{\partial P}{\partial z}+_v\frac{\partial^2 u_z}{\partial x^2}+\frac{\partial^2 u_z}{2}+\frac{\partial^2 u_z}{2} \tag{4}$$

where *ux*,*uy*, *and uz* are the velocity components of the flow field concerning the local coordinate system set within the robot; P is the fluid pressure; ρ is the fluid density; v is the dynamic viscosity coefficient. The presented numerical simulations are performed using Reynolds-averaged Navier-Stokes (RANS), and in RANS, the Reynolds stresses require modeling and closure. Here, the k_ω model is applied to the calculation. The SST k_ω turbulence model is a two-equation eddy-viscosity model commonly applied for hydro- and aerodynamics [10] [11].

$$\frac{\partial k}{\partial t}+U_j\frac{\partial k}{\partial x}=_{P_k}-\beta^* k\omega+\frac{\partial}{\partial x}\left[\left(\nu+\sigma_k\nu_T\partial x\right]_j{}_j\,dk\right. \tag{5}$$

$$\frac{\partial \omega}{\partial t}+U_j\frac{\partial \omega}{\partial x_j}=\alpha S^2-\beta\omega^2+\frac{\partial}{\partial x_j}\left[\left(\nu+\sigma_\omega\nu_T\right)\frac{\partial \omega}{\partial x_j}\right]+$$

$$2\left(1-F_1\right)\sigma_{\omega 2}\frac{1}{\omega}\frac{\partial k}{\partial x_i}\frac{\partial \omega}{\partial x_i} \tag{6}$$

$$F_2=tanh\left[max\left(\frac{2\sqrt{k}}{\beta^*\omega y},\frac{500\nu}{y^2\omega}\right)\right]^2\Bigg] \tag{7}$$

$$P_k=min\left(\tau_{ij}\frac{\partial U_i}{\partial x_j},10\beta^* k\omega\right) \tag{8}$$

$$F_1=tanh\left\{\left\{min\left[max\left(\frac{\sqrt{k}}{\beta^*\omega y},\frac{500\nu}{y^2\omega}\right),\frac{4\sigma_{\omega 2}k}{CD_{k\omega}y^2}\right]\right\}^4\right\} \tag{9}$$

$$CD_{k\omega}=max\left(2\rho\sigma_{\omega 2}\frac{1}{\omega}\frac{\partial k}{\partial x_i}\frac{\partial \omega}{\partial x_i},10^{-10}\right) \tag{10}$$

$$\phi=\phi_1F_1+\phi_2\left(1-F_1\right) \tag{11}$$

were $\alpha_1=\frac{5}{9};\alpha_2=0.44;\beta_1=\frac{3}{40};\beta_2=0.0828;\beta^*=\frac{9}{100};$

$\sigma_{k1}=0.85;\sigma_{k2}=1;\sigma_{\omega 1}=0.5;\sigma_{\omega 2}=0.856.$

2.1.2 Geometry Generation

The core design of the AUV draws inspiration from the squid's distinctive Motion and physical attributes, as shown in Figure 1. Specifically, a squid propels itself by intaking water into its mantle and forcefully expelling it through a siphon, adjusting its direction to enable effective turning [8]. The AUV emulates this by drawing water through a pump at its end and expelling it to achieve propulsion. Similar to the squid's siphon mechanism, the direction of the AUV can be controlled by adjusting its bionic rudders, which allows for repositioning the direction of the water pump. This dynamic feature minimizes noise production by the propellers and reduces the risk of seaweed entanglement, thereby enhancing the operational safety of the AUV in a coral reef environment. Moreover, incorporating bionic rudders, unlike traditional end-located rudders, allows a smaller turning radius. The rudder can exert significant force by pushing water around itself to adjust the AUV's orientation, enhancing maneuverability—a crucial quality in the intricate and delicate coral reef ecosystem [12].

On the physical dimension side, the AUV adopts a hydrodynamic shape similar to the squid, transforming the tentacles used for preying into bionic rudders and embracing the streamlined form of the squid. The squid's head, a filled cone shape, yields a streamlined design that minimizes pressure drag at the expense of viscous drag when moving [17]. This similar approach is employed in the AUV but with the length of the cone further optimized using CFD analysis. This fusion of biological inspiration and cutting-edge computational techniques results in an advanced design that leverages nature's solutions to fluid dynamics.

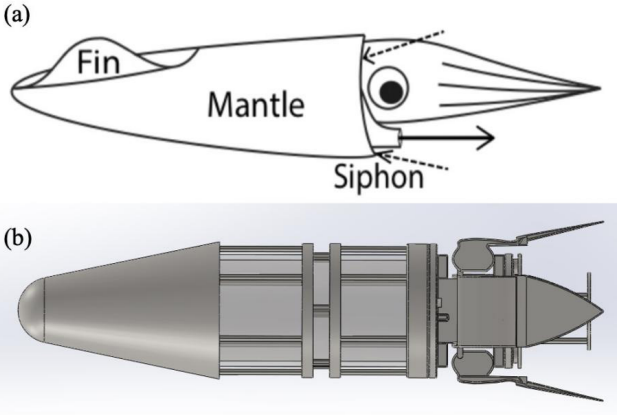

Figure 1: Comparison of squid and the AUV proposed: (a)Dimensions of squids [8] (b) Dimensions of the AUV

The control model utilized in this study is the initial AUV prototype, as shown in Figure 2, which does not include the head extensions. First and foremost, the parts obtained

from the 3D designing and printing were inserted in SolidWorks Assembly and then later constructed using mates, corresponding to their actual position. As CFD analysis would only examine the exterior shell of the AUV, and in complete disregard of the actual mass of the robot, the control center and many electronics were taken out and simplified to their purest form. Before the analysis, complex structures such as bolts, motors, or wiring were disregarded, as they do not have a noticeable influence on the results but significantly increase the time complexity of the mesh changes during analysis. Ultimately, the simplified version of the AUV's Computer-aided design is obtained. This is the basic model that the analyses below will be based on, aiming to improve the design.

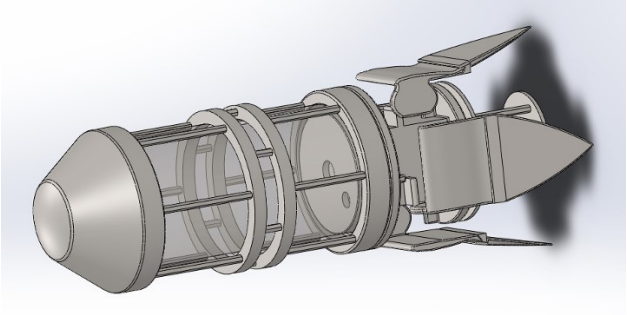

Figure 2: Geometry of the AUV

2.1.3 Computational Domain and Boundary Conditions

In CFD simulations, the fluid medium interacting with the object of study is divided into a grid-like structure of small cells. These cells represent the fluid flow and its interaction with the object. The number of cells in the grid directly influences the simulation's computational complexity and the results' accuracy. The SolidWorks assembly file for the analysis is initially exported as a Parasolid file. This file format is compatible with the SpaceClaim software environment, allowing the exported model to be imported into SpaceClaim for further processing. In this case, the analysis domain is an outer shell modeled as a rectangle. The dimensions of this rectangle are five times the length (L) of the Autonomous Underwater Vehicle (AUV) model along the direction of the fluid flow and three times the length (L) along the span direction, starting from the widest point of the AUV. Here, L denotes the length of the 3D CAD model of the AUV, measured at 407mm. Choosing such a domain size, though computationally intensive, is done for specific reasons. The wake effect is a flow phenomenon characterized by a region behind the AUV that undergoes disturbances due to the vehicle's presence. This effect arises due to the inherent viscosity of fluids, leading to various outcomes, including turbulence, recirculation, and alterations in pressure distribution [2]. By expanding the analysis domain, CFD simulations can precisely investigate the wake region, enabling comprehension of the resulting impact on the hydrodynamics of the AUV.

The boundary conditions, illustrated in Figure 3, were imposed as follows: The front side, positioned in front of the robot, was designated as a velocity inlet, through which the fluid enters with a velocity corresponding to the robot's speed, which was approximated to 0.17m/s. The opposing side, facing the back of the robot, was identified as the outlet, representing an outflow boundary condition. This condition is implemented at the exit of the computational domain, which corresponds to the outer shell of the analysis, simulating the region where the fluid exits the system. The remaining four sides are referred to as sides and imposed as free-slip boundary conditions. Lastly, all surfaces on the AUV are treated as non-slip boundary conditions.

Table 1: Grid Independent Study

0.292m	616661	0.2456	0.0710
0.120m	2135614	0.2521	0.0724
0.097m	2905593	0.2537	0.0726

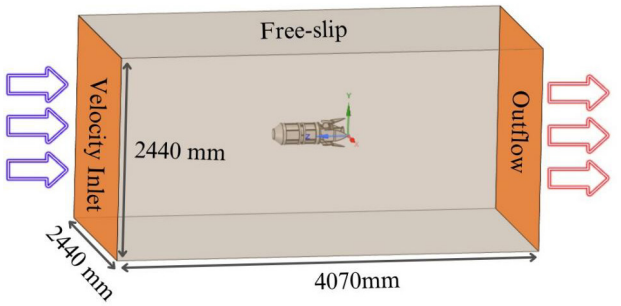

Figure 3: Computation domain and boundary conditions

2.1.4 Mesh and Grid Independence Study

Establishing an optimal mesh resolution within the computational domain is crucial in numerical analyses. Augmenting the concentration of mesh elements inherently refines the precision of the resultant outputs, albeit at the cost of escalated computational expenditure and resource allocation. To ascertain the veracity of the meshing methodology, the current investigation conducted numerical calculations utilizing three distinct mesh densities facilitated through ANSYS Meshing and juxtaposed the respective numerical outputs. The aim was to substantiate the proposition that alterations in mesh density bear minimal influence on the resultant data. In this research endeavor, the meshing procedure was employed on the default robotic configuration, which omits the cranial extension yet incorporates a 45-degree rudder extension. This specific configuration was

elected based on the antecedent experimental trial that authenticated its capability to yield the minimum turning radius.

Upon inspection of the various scenarios in Table 1, it becomes discernible that alterations in the mesh density within the framework of CFD simulations do not engender significant consequences, particularly beyond a mesh count threshold of 2 million. As a result, it is deduced that subsequent CFD analyses, predicated on the elected mesh size of 0.120m—corresponding to approximately 2.1 million mesh elements for this specific robotic configuration—remain impervious to variations in the selected mesh quality. Hence, the mesh configuration is selected to be 0.120m, as demonstrated in Figure 4.

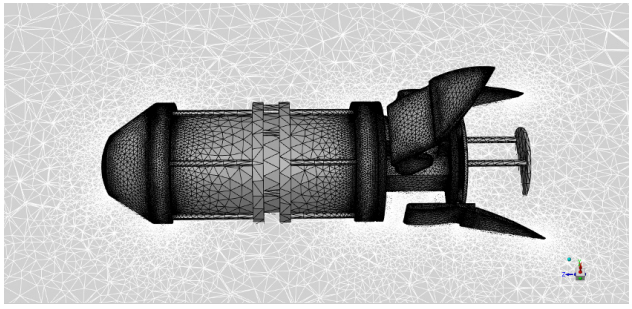

Figure 4: An example of the Mesh for calculation

2.1.5 Numerical Setup and Calculation Process

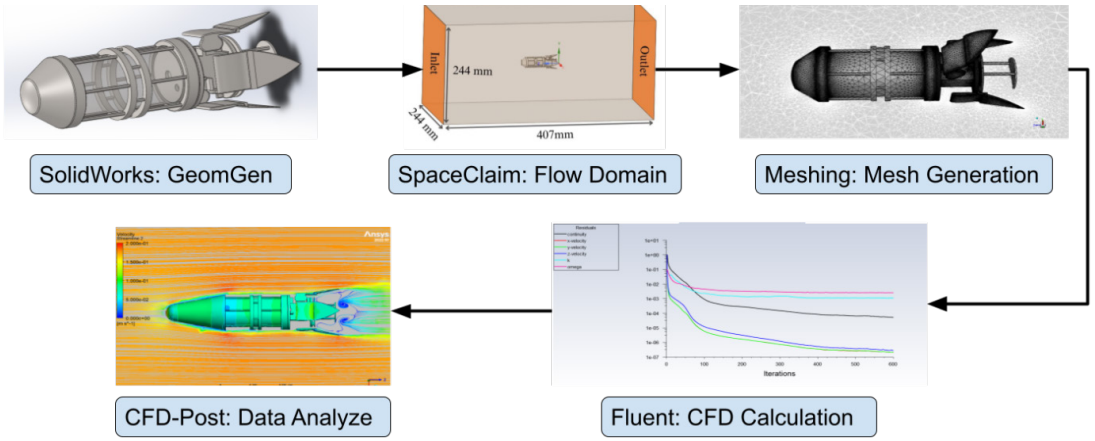

Figure 5: Flowchart of the CFD

All procedures of CFD, illustrated in the flow chart in Figure 5, were executed utilizing the SolidWorks and ANSYS software suites, beginning with the selection of Fluent within the workbench. This integrated toolset encompasses various functionalities, from three-dimensional modeling and mesh generation to numerical computation and subsequent data analysis.

Post the generation of the outer casing using SpaceClaim, the Parasolid components are eliminated, rendering the shell as the sole remaining entity within the digital workspace. In the robot's spatial orientation context, the face orienting toward the robot's head is denominated as the inlet. In contrast, the face towards the robot's posterior is identified as the outlet. The lateral surfaces encapsulating the robot are collated and collectively designated as "sides." All of these boundaries are selected to remain concealed. The bionic squid itself is classified as the AUV. Subsequently, the Workbench software autonomously populates the resultant boundary into the Mesh application. Within the Mesh application, the physics preference is designated CFD, and the solver preference is determined as Fluent. The order of elements is linear, with a deliberate element size of 0.12m, as determined from the Grid Independence Study. Mesh autonomously fabricates a grid and simulates the fluid dynamics following these specifications. The mesh data is then ingressed into Fluent, the platform where the principal hydrodynamic analysis will be enacted.

In this investigation, liquid water was selected as the working fluid, with a density of 998.2 kg/m^3 and a viscosity of 0.001003 kg/$m\,.\,s$, values sourced from the ANSYS data library, as shown in Figure 6.

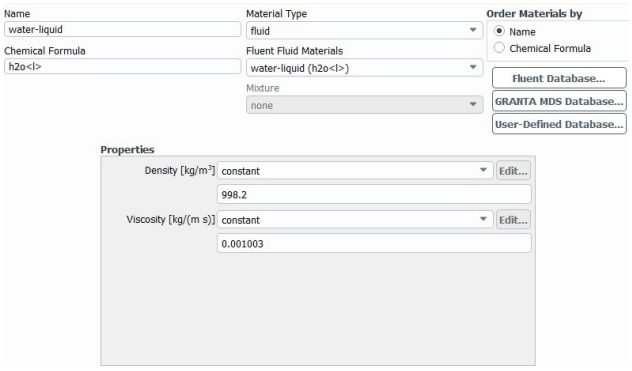

Figure 6: Settings of fluid properties

Subsequently, an additional examination, set up in the interface shown in Figure 7, is undertaken on the drag force exerted on the robotic entity during its Motion. The drag force acting in the *z*-direction is meticulously tracked and quantified in Newtons (N), and this particular value is outputted as a file. This value is then represented graphically, enabling a direct visual assessment of its pattern or trend. This visual representation provides an intuitive understanding of the force dynamics that the AUV experiences during operation.

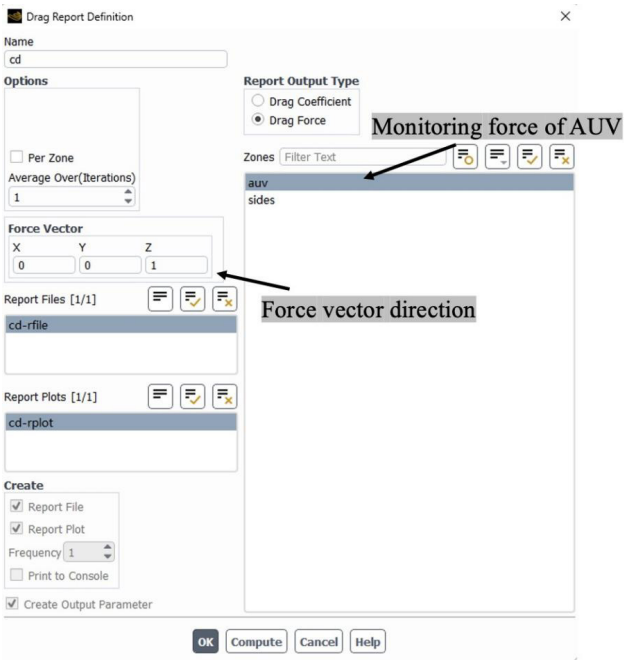

Figure 7: Drag report definition

The residuals are adjusted to bolster precision. Absolute criteria—namely continuity, x-direction velocity, y-direction velocity, z-direction velocity, k (turbulent kinetic energy), and omega (specific dissipation rate)—are regulated to an exacting value of 10−5 in the Fluent interface. This procedural step guarantees an accurate solution within the computational analysis, thereby increasing the reliability and accuracy of the results.

This code relies on an unstructured body-fitted grid with collocated pressure and velocity nodes. The numerical algorithm is based on the SIMPLE algorithm. A second-order upwind scheme discretizes the convective terms in the momentum equation. The pressure-correction under-relaxation factor is configured at a value of 2.0, facilitating accelerated calculations, thereby rendering the methodology apt for the extensive array of cases scrutinized in the subsequent sections [15].

In the aftermath of the initialization computation spanning all zones, the CFD simulation is primed for execution. The calculation is subjected to approximately 600 iterations, depending on the complexity of the AUV model, enabling the solution to reach convergence before the commencement of the analytical operation; as shown in Figure 8, the drag force experienced is chosen as the parameter to corroborate the convergence.

After the simulations' completion, the generated results are imported into the ANSYS CFD.

Post-processing module through the ANSYS Workbench. This module facilitates the construction of various types of visual representations, including pressure contours and streamline plots, which analyze and compare the performance of various designs. The color configuration within the graphical depictions, represented by the figure's legend, is consistent across all comparisons. This adherence to uniformity in color representation ensures an unbiased and straightforward comparison across various design performances.

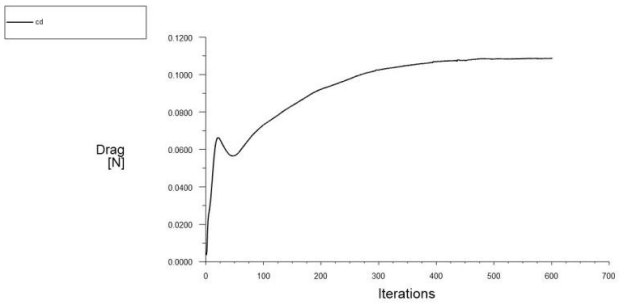

Figure 8: Variations of drag force concerning the iterations

2.2 Experimental Test

2.2.1 Experiment Apparatus

The AUV's components designed in the SolidWorks CAD software are realized through various 3D printing techniques. These include using a 3D PLA printer, a 3D UV curable resin printer, and a 3D TPU printer, each contributing to the overall design with their unique material properties. Furthermore, additional construction materials like acrylic and wood are incorporated into the design. The spatial organization of these materials is mapped out on AutoCAD and actualized using a laser cutter, with its operation shown in Figure 9(a).

Figure 9: Illustration of apparatuses: (a)laser cutter in operation, (b)solder station

The electronic subsystems of the AUV is integrated through a soldering station, as shown in Figure 9(b), facilitating the secure connection of the various components and their corresponding pins.

A water tank filled with fresh water is chosen as the experimentation location, effectively mimicking the operational conditions of the AUV. The recording of the experimental trials is documented via a stationary camera, which provides a comprehensive view of the test environment, as illustrated in the figure.

10. a half-meter ruler is included within the frame as a reference for distance measurements.

2.2.2 Structure Sesign of AUV

The AUV consists of three components: the head, the control center, the steering, and the dynamic section, with the overview shown in Figure 11.

The decision to design the AUV with a conical shape and a spherical front for the *head* is rooted in biomimicry, specifically drawing inspiration from squids, as depicted in Figure 12. Should a tapered or pointy head be employed, the water resistance—dynamics viscosity of 1 centipoise at 20°C and

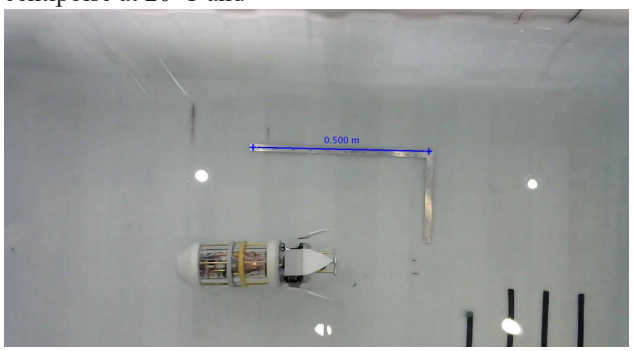

Figure 10: Illustration of the camera field of view

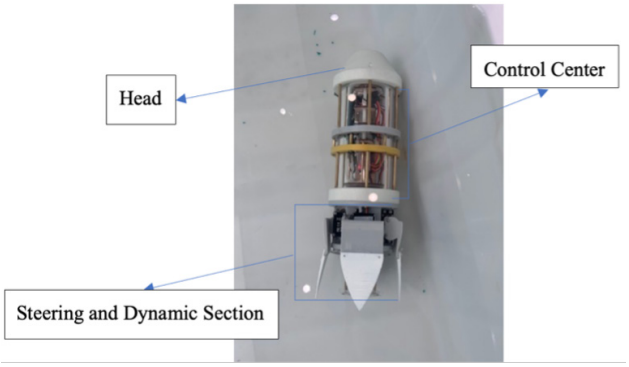

Figure 11: Structure of the AUV

A 1000 kg/m^3 density would exert a significant force at the robot's rear. This would introduce a disparity in the forces acting on the robot's front and rear, culminating in pronounced pressure drag and escalating energy consumption.

Conversely, a spherical head design allows the robot to traverse through the water with reduced resistance, creating a more substantial wake behind it and thus diminishing the frictional forces exerted on it. The precise dimensions of the head were optimized in the CFD section, ensuring the design achieves the most favorable hydrodynamic performance.

The inherent characteristics of 3D printed UV curable resin, which, in its solid state, exhibit an intricate and rough microscopic texture. This texture facilitates the potential escape of water and its gradual permeation inward, particularly when subjected to high water pressure. Given that all electronic components are housed within the control center, it necessitates a zero-tolerance policy towards water leakage, as such ingress would inevitably lead to detrimental effects on the electronic system. To ensure the sealing ability of the control center, a 15mm indentation inside the head shown in Figure 13 was utilized to connect the acrylic tube. Additionally, a rubber ring gasket was added to further reduce the gap between the head and the cylinder, which, when pressed, will occupy the vacant spaces.

The core unit of the *control center*, also regarded as the heart of this system, is a cylindrical tube composed of acrylic, with the distribution shown in Figure 14. The tube's dimensions are meticulously chosen to maintain structural integrity, with a thickness of 3mm. This selection ensures a delicate balance between durability and mass, making it lightweight yet robust enough to securely house sensitive electronics.

The cylinder serves dual functions, both organization and protection. It is intended to efficiently manage and contain a suite of electronic components. The layout and design of the electronics' placement within the tube are

meticulously strategized for optimal performance and to reduce interference amongst the devices. However, two main components are strategically kept external to this acrylic tube - the water pump and the servo motors. Given the operational requirements of these components and their physical

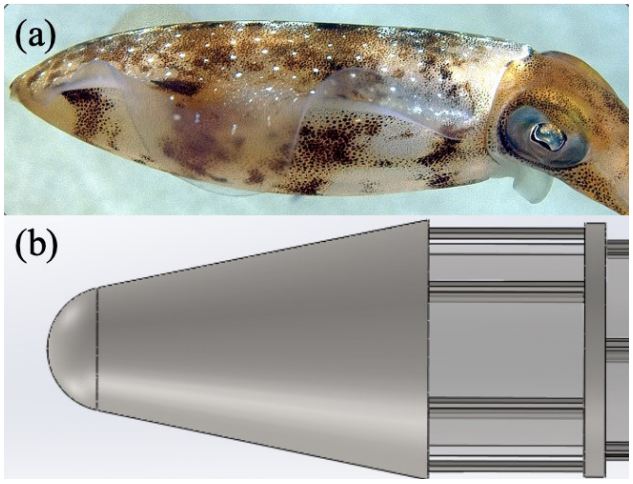

Figure 12: Head inspired by submarine: (a) head of a squid [18] (b)head of the AUV

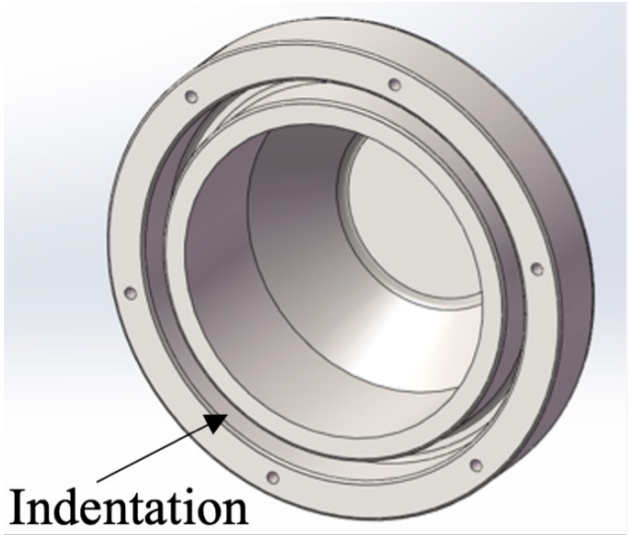

Figure 13: Illustration of the indentation of the head

interactions with the environment, it is practical to position them outside the control center tube. The protection aspect of the cylinder's role is paramount. One of its primary defensive duties is to shield the delicate electronic components from the potential harm of water infiltration.

The control center design employs two identical 3D-printed rings positioned externally on the acrylic tube. These rings serve as interfaces for connecting copper standoffs, forming the protective cage around the acrylic tube. As depicted in Figure 15, the axial dimension of the acrylic tube surpasses the length of the copper standoffs and the additive manufactured components. This configuration is engineered to effectuate the compression between the apex and terminal of the control center, guaranteeing the transmission of mechanical forces primarily to the acrylic structure. This design approach minimizes the potential ingress points for water by exerting pressure on the rubber gaskets, thereby ensuring an enhanced level of fluid-tight integrity.

The terminal portion of the control center represents another industrially fabricated component, with the front-back view shown in Figure 16, realized through UV curable resin. The side orienting toward the control center exhibits a concave feature mirroring the head's. In the terminal part of the control center, there are two apertures. The 16mm aperture accommodates the waterproofed electrical conduits from the servo motors and the water pump within the steering and dynamic section. On the other hand, the 10mm perforation is devised to expose the water conduit from the peristaltic pump to the external environment, allowing for uninhibited interaction with water. These

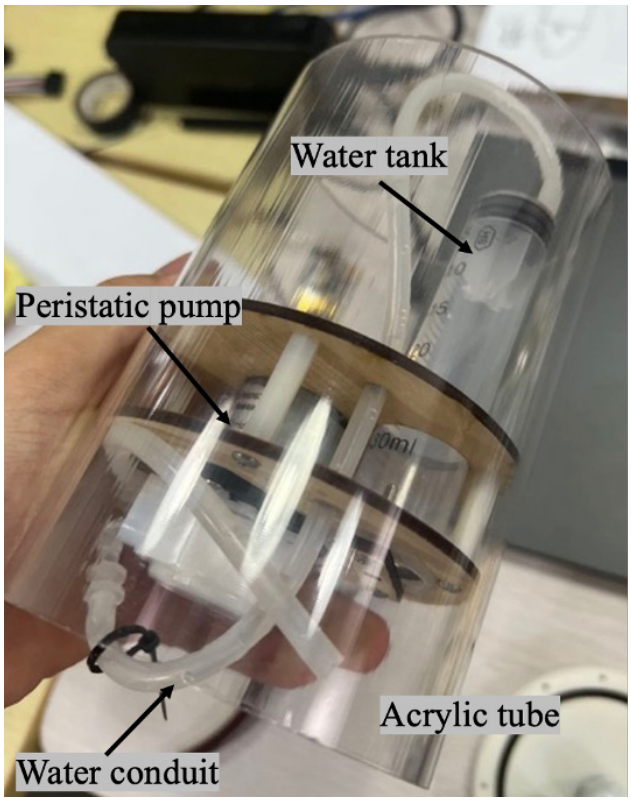

Figure 14: Photograph of the acrylic tube and intake system

openings are sealed using screwable rubber gaskets to ensure a robust, leak-proof interface.

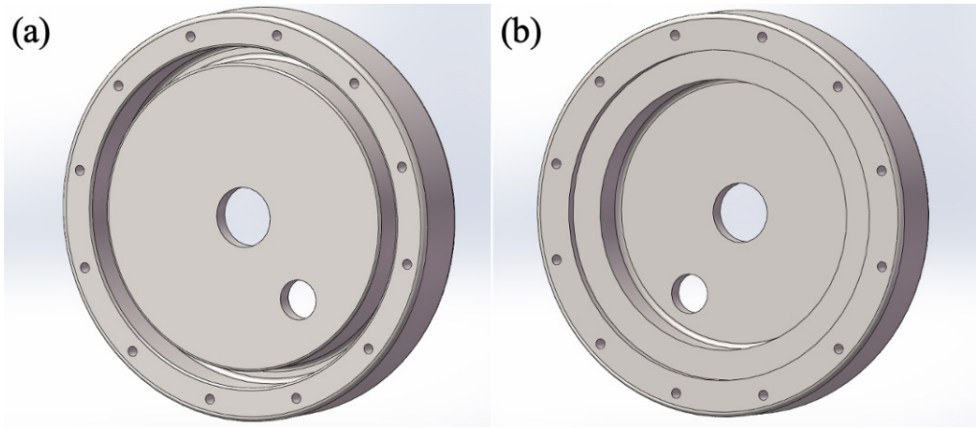

Figure 16: Illustration of the control center's end: (a)front view (b)back view

Given the direct exposure of these two apertures to the aquatic environment and the potential for minuscule gaps to form around the wire conduits, supplementary waterproofing strategies are essential to enhance the system's resilience. To address this challenge, hot glue is applied at the wire intersections and the contact points between the conduit and the terminal of the control center. This acts to solidify the positioning of the wires. Following the curing of the hot glue, a water-sealing glue is circumferentially around the cables to preclude the possibility of leakage.

The rudder configuration, situated within the steering and dynamic section as depicted in Figure 17, is designed to optimize hydrodynamic efficiency, aiming to minimize drag when in a retracted state and maximize maneuverability when extended. This setup consists of a primary 3D-printed rudder.

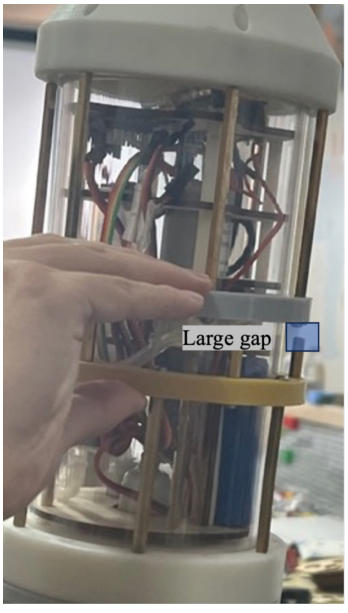

Figure 15: Illustration of structural integrity

component incorporates a connection structure oriented perpendicularly to the rudder surface. An additional extension element, fabricated using Thermoplastic Polyurethane (TPU)—renowned for its flexibility and resilience—is attached to the rudder's terminus. This flexible extension enhances the drag force exerted on the rudder in its aquatic environment, improving its steering effectiveness. This TPU-based extension is designed with dual 3mm perforations positioned at its leading edge, facilitating secure attachment to the rudder surface.

The steering and dynamic section of the AUV possesses a complex structural configuration, as demonstrated in Figure 18. The larger circular face of this structural component serves as the interface for the connection between the rear portion of the control center and the steering and dynamic module. This face features six apertures, each accompanied by a cylindrical extension with a length of 2mm. These extensions play a critical role in ensuring the free flow of water towards the tubing of the peristaltic pump. This flow facilitates the appropriate water routing to storage and controls the robot's buoyancy operations, namely surfacing and submerging.

The structural component of the robot features a through-hole with a diameter of 40mm, discernible in both frontal and rear views. This substantial aperture serves multiple purposes, accommodating the servo motors and water pump wiring while contributing to reducing unnecessary mass from the robot. The terminal segment of the robot integrates two acrylic cylindrical structures, each exhibiting a thickness of 2.8mm, which are conjoined with the steering mechanism. The minor of the two cylinders fortifies the efflux pipe associated with the water pump system. This design choice guarantees the symmetrical expulsion of the water stream, an essential element in sustaining equilibrium in the robot's maneuvers. This is actualized via a circular perforation within the smaller cylinder, through which the outlet conduit from the water pump is extended. The water pump in the robotic system incorporates a filter screen secured in place with a zip-tie,

as depicted in Figure 19. This filtration component serves a critical function by preventing the ingress of particulate matter or other solid debris, which could potentially impair the function of the internal motor within the water pump.

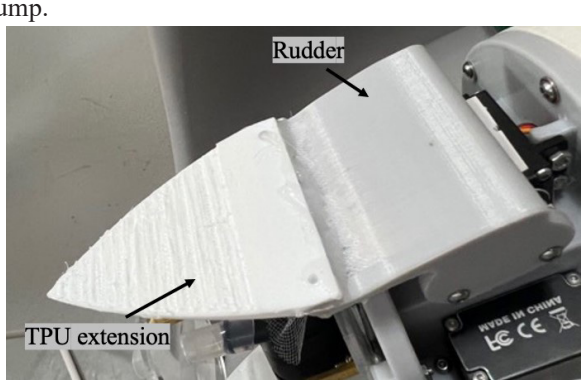

Figure 17: Photograph of the TPU rudder extension

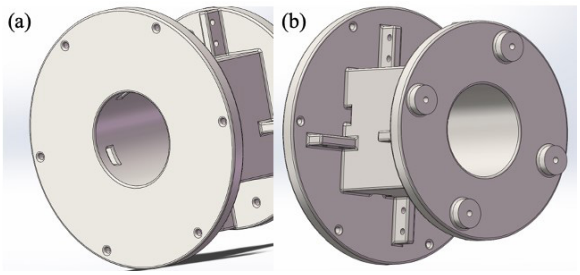

Figure 18: Illustration of the steering and dynamics section: (a) front view, (b) back view

Such a filter is essential in maintaining the operational efficiency and longevity of the pump, particularly when deployed within environments that may contain a substantial quantity of suspended particles or solid debris.

Figure 19: Filtered water pump

2.2.3 Program Design

As the experiments will be carried out in freshwater and water tanks to simulate the actual environment, the radio transceivers for both onshore and offshore were selected to be the default antenna of the Lora ESP 32 motherboard. This antenna has a frequency of 868~915MHz and receiver sensibility of up to 139dBm [9]. With such, the communication range could be calculated using the Beer-Lambert Law and

The seawater attenuation empirical relation:

$$I(d) = 10 \times e - a_f d \tag{12}$$

$$a_f \approx 0.11 \times f_{1.33} \tag{13}$$

where I(d) is the intensity, measured in dBm, at a distance of d; I0 is the initial intensity, measured in dBm; af is the absorption coefficient of seawater concerning the frequency of f; f is the frequency of the wave; d is the distance.

For the transceiver to successfully receive the signal, the intensity I(d) must exceed a threshold of

139dBm. By employing the exponential attenuation law, the communication range for the frequencies [868MHz, 915MHz] is calculated to fall within the narrow range of [2.7cm, 2.8cm] in seawater, rendering it unsuitable for underwater communication. In contrast, using freshwater for testing offers a significant advantage due to its lower salinity, resulting in reduced conductivity and absorption of radio waves. Consequently, the attenuation in freshwater is often approximated to be an order of magnitude lower, extending the effective range of the Lora ESP 32 transceiver to between [27cm and 28cm], which is sufficient for testing purposes [4].

Two motherboards are utilized—one inside the robot and another as part of the controller. The overall programming design follows a classical robot control program, employing a while loop that continuously operates while searching for demands from the controller using if statements, with the program logic for onshore and AUV shown in figures A.1 and A.2, respectively. Upon receiving a command, the Lora ESP 32 motherboard sends a signal using the accompanying Lora transceiver. Subsequently, the motherboards inside the robot receive and decode the message, converting it into a command to be executed by the motors.

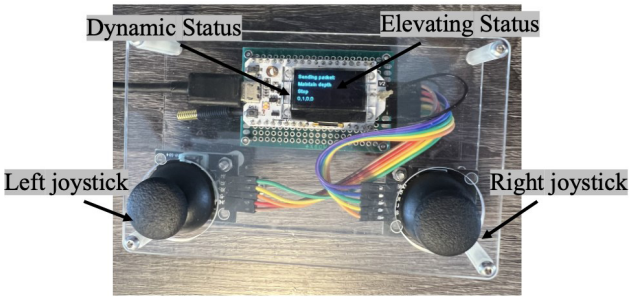

Figure 20: Photograph of the controller

The controller depicted in Figure 20 features two joysticks, both connected to the Lora ESP32 motherboard. The left joystick governs the AUV's vertical and forward movements: pushing up and down controls surfacing and sinking while tilting left controls forward speed, and a right push activates an "all-stop" function by extending all rudders, thereby increasing pressure drag. The right joystick, in contrast, controls individual rudder extension, with the direction of the tilt determining the specific rudder affected. The onboard LED screen on the Lora ESP32 conveys the AUV's dynamic status, including movement ("All Stop," "Stop," or "Ahead: n" where "n" is the pump power within [0:255]) and elevation ("Maintaining Depth," "Surfacing," or "Sinking"), providing essential feedback to the operator.

2.2.4 Motion Controlling

A conduit composed of pliable material bridges the peristaltic pump to the external environment and the internal water reservoir. Upon submersion, the robot capitalizes on the ambient water, drawing it into the reservoir, dispelling internal air pockets and augmenting its aggregate density.

Carefully calibrated counterweights ensure that even a minimal increment in gravitational force can induce the robot's descent. Once fully submerged, the overlying water pressure contributes to the amplification of the downward impetus. The captive water within the reservoir is methodically discharged until the forces of buoyancy and gravity reach equilibrium, culminating in a zero net force. Consequently, the robot acquires the capacity to maintain a stable position within the water column at a predetermined depth. Resurfacing is achieved by expulsing the water from its internal reservoir via a peristaltic pump, bolstering the buoyant force.

The elevation and submersion functionality allows the robot to fully immerse and emerge within a water body. This function enables the robot to execute a strictly vertical translational motion independent of any lateral displacement, which is beneficial when operating within restricted spaces. The accuracy of the displacement executed via this method surpasses conventional diving or surfacing techniques, as the displacement can be calculated based on the water intake or discharge duration. Conversely, post-diving positional maintenance is challenging due to residual momentum. Furthermore, levitation, facilitated by the buoyant force, minimizes disturbance to the marine ecosystem, as it operates silently, mitigating the risk of alarming the marine inhabitants.

The steering and dynamic module of the robot deploys four rudders - two on the lateral aspects and two on the dorsal and ventral surfaces. These four rudders collectively orchestrate the overall navigation of the robot. Upon deployment, the rudder expands its surface area exposed to the aquatic current, accruing drag force, which consequently pivots the robot in the counter direction to the rudder's orientation.

The utility of turning is self-explanatory; it equips the robot with the capability to autonomously alter its course or destination post-deployment. Nevertheless, the capabilities of diving and surfacing also hold pivotal importance. Despite some functional overlap with the sinking and surfacing mechanism, the diving and surfacing feature facilitates smooth adjustment of the robot's vertical positioning. Furthermore, the judicious application of these mechanisms empowers the robot to traverse intricate tunnel networks necessitating vertical displacement.

3 Theory Analysis: Hydrodynamic Forces of AUV

When traversing in water, an AUV is subject to complex hydrodynamic forces, predominantly characterized by drag and lift forces. The energy consumption of the AUV is intrinsically tied to counteracting these forces, with the drag force being a principal contributor. Therefore, minimizing drag becomes a critical consideration in the design and operation of AUVs.

Drag force is a resistance force exerted on an AUV when it moves through a fluid. This force arises from fluid particles' continuous, random motion that collide with the AUV, creating pressure. When the AUV moves, it disrupts the equilibrium of this pressure, leading to a higher pressure on its front side and a lower one on the back. The resulting pressure difference forms the drag force, opposing the

AUV's movement. This is a key factor in AUV design, impacting energy efficiency and performance [1]. When the AUV submerges into stationary water, a hydrostatic pressure gradient is established due to the weight of the overlying fluid. The pressure exerted on the surface of the AUV results from the ongoing collisions of fluid particles against its surface, exerting a force normal to the AUV's surface. Such a process is illustrated in Figure 21(a).

In the dynamics context, the motion of the fluid in the vicinity of an AUV and its surface gives rise to a tangential shear force, as shown in Figure 21(b), which is a consequence of the viscosity of liquids and the application of the no-slip condition at the AUV's surface. The no-slip condition states that fluid particles in direct contact with the surface of the AUV will have zero relative velocity concerning the AUV. In other words, when a fluid

flows over the AUV's surface, the fluid particles closest to the surface move at the same velocity as the surface itself. This phenomenon accurately represents the behavior of viscous fluids, which occurs due to the frictional forces between the solid surface and the fluid. In the specific case of this study, the AUV's surface was considered a no-slip region, as the fluid under consideration is liquid water [5].

From the normal and shear force diagram, one could directly visualize the drag and lift forces resulting from the shear and pressure.

$$dF_D = -P\,dA\cos\theta + \tau_w\,dA\sin\theta$$
$$dF_L = -P\,dA\sin\theta + \tau_w\,dA\cos\theta \quad (14)$$

The AUV is a bluff body, which implies that it causes the separation of fluid flows over a significant portion of its body due to its shape. As a result, the drag force primarily originates from pressure drag,

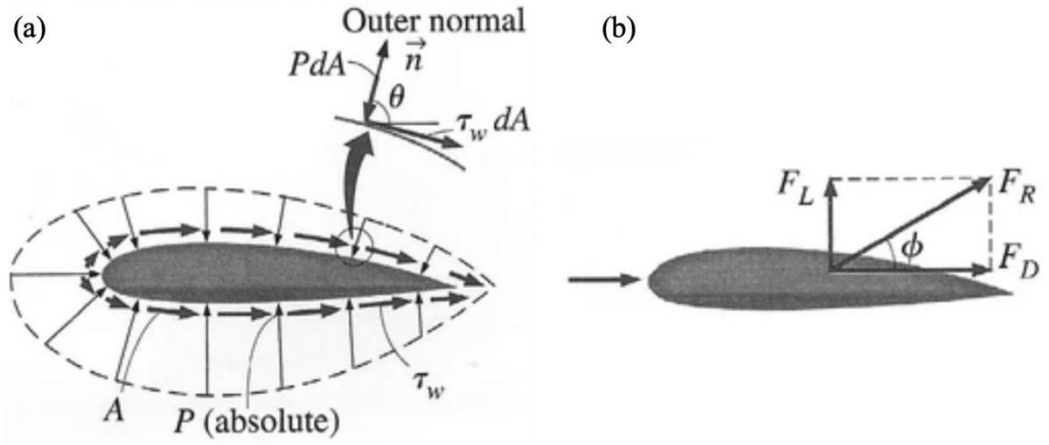

Figure 21: Schematics of drag forces: (a)pressure drag[5] (b)viscous drag[5]

since bluff bodies experience higher pressure at the front of the body rather than the rear. This disparity creates a non-recovery pressure on the downstream or rear side of the AUV. The pressure drag becomes particularly pronounced when the fluid flow is separated and creates a low-pressure region behind the AUV. On the other hand, the friction drag that occurs due to the fluid's viscosity depends on the fluid is viscosity coefficient and the surface layer profile of the AUV, represented by the gradient dU/dy. Here, U represents the fluid velocity at the surface, which, due to the no-slip condition, is equal to the velocity of the AUV. Meanwhile, y represents the direction normal to the surface of the AUV. Consequently, the intensity of the shear drag is influenced by whether the boundary layer is laminar or turbulent.

Another significant hydrodynamic force encountered by an AUV is the lift force, which is generated perpendicular to the direction of fluid flow. Lift in an AUV can manifest in two primary orientations, responsible for vertical movement (rising or sinking) and turning. Lift is predominantly a result of suction forces arising due to a negative pressure zone created by the flow of fluid over and under specific surfaces of the AUV. This pressure differential can produce forces that induce changes in direction or depth.

At the profile that results in zero lift incidence, there will be an equivalent fluid path over and under, or left and right, of the AUV's surfaces. This uniformity in pressure distribution means that no lift forces are generated, leading to a lack of vertical or lateral movement. Consequently, the AUV continues straightly, unaltered by lift dynamics [3].

4 Hydrodynamic Analysis Based on CFD Simulations

Within this section, two distinct investigations are conducted to optimize the hydrodynamic performance of the AUV, whose current design is inspired by the dimensions of squids.

First, the length of the head's conical section is investigated. Determining the optimal length for this feature is essential, as it can significantly affect the drag forces experienced by the AUV, yielding a higher energy efficiency and maneuverability. The question is to ascertain the length that yields the most favorable balance, reducing drag while maintaining other desired hydrodynamic properties.

Subsequently, the study introduces an innovative approach to minimize pressure drag, a significant component of the total drag force. This method employs a disk before the robot to create a cavity region. The formation of this cavity reduces the pressure disparity between the front and

rear of the AUV, as well as the interaction between fluid and head. This strategic manipulation of fluid dynamics represents a novel avenue for enhancing the efficiency and maneuverability of underwater robotic systems.

4.1 Effect of head's length on the hydrodynamics of AUV

In all circumstances, reducing drag force is a critical factor for any AUV, as it yields numerous performance advantages. Firstly, it enhances the energy efficiency of the robot. Drag force consumes energy and significantly affects AUVs' propulsion systems, necessitating additional energy to overcome this resistance. The design presented in this paper focuses on a miniature AUV with dimensions of approximately $400mm \times 200mm \times 200mm$. Although suitable for expeditions within sophisticated coral reef ecosystems, this compact size limits the capacity for large battery power sources. The robot utilizes a 2200mAh 12V battery. By reducing drag force, the head extension design alleviates the strain on the battery, enabling prolonged operation before requiring a recharge.

Secondly, minimizing the aggregate drag force experienced by the AUV results in a consequent enhancement in its hydrodynamic maneuverability. This optimization facilitates more precise and efficient operations within intricate coral reef ecosystems, thereby reducing potential biomechanical disturbances and preserving the delicate coral structures.

The head shape of the AUV is designed by sketching the cross-section of the filleted cone in Solidworks and creating a revolve feature with the axis of rotation being the height.

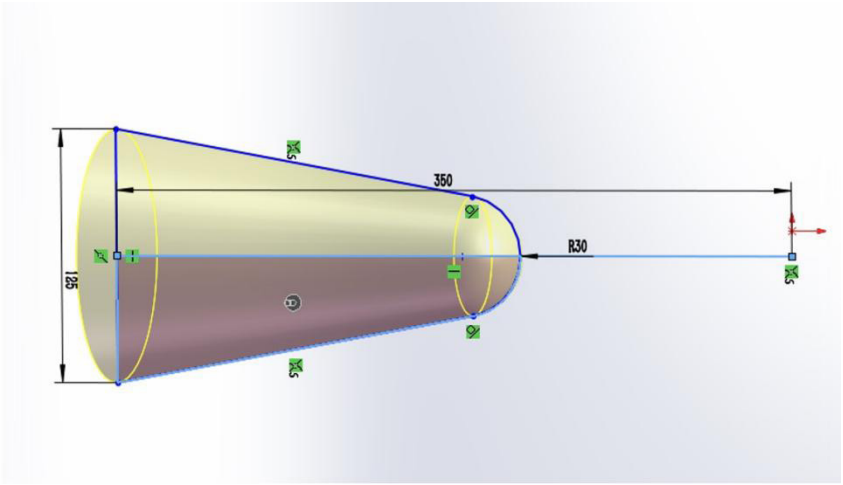

Figure 22: Illustration of the length of the head

By manipulating the height of the filleted isosceles triangle demonstrated in Figure 22 within the range of (150 mm, 200 mm, 250 mm, 300 mm, 350 mm, and 400 mm), the actual height of the head will be obtained as (102.00 mm, 129.42 mm, 156.31 mm, 182.91 mm, 209.34 mm, 235.67mm), allowing one to observe the co-relation between the viscous/pressure drag force experienced and the length of the head.

Table 2: Drag forces of AUV with different head lengths

	Head's length(mm)	Pressure drag(N)	Pressure drag pct.	Viscous drag(N)	Viscous drag pct.	Total force(N)
Case L1	102.00	0.1025	89.65%	0.0118	10.35%	0.1143
Case L2	129.42	0.0980	88.66%	0.0125	11.34%	0.1105
Case L3	156.31	0.0950	86.60%	0.0147	13.40%	0.1097
Case L4	182.91	0.0927	85.42%	0.0158	14.58%	0.1085
Case L5	209.34	0.0917	84.74%	0.0165	15.26%	0.1082
Case L6	235.67	0.0915	84.32%	0.0170	15.68%	0.1085

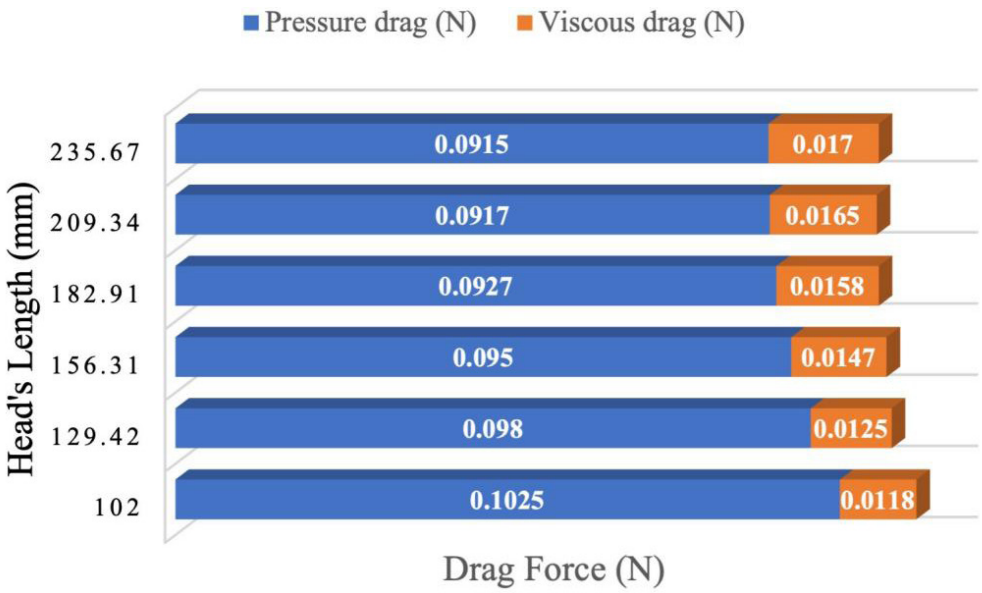

Figure 23: Contributions of drag forces

Figure 23 indicates a distinct trend where an increase in the length of the head corresponds to a noticeable decline in pressure drag, concomitantly with an escalation in viscous drag. This phenomenon can be attributed to the resultant aerodynamic profile becoming increasingly streamlined, albeit at the expense of an augmented surface area. Consequently, the configuration exhibiting the minimal drag force is Case L5. Notably, the models Case L6 and Case L4 demonstrate quasi-symmetrical results.

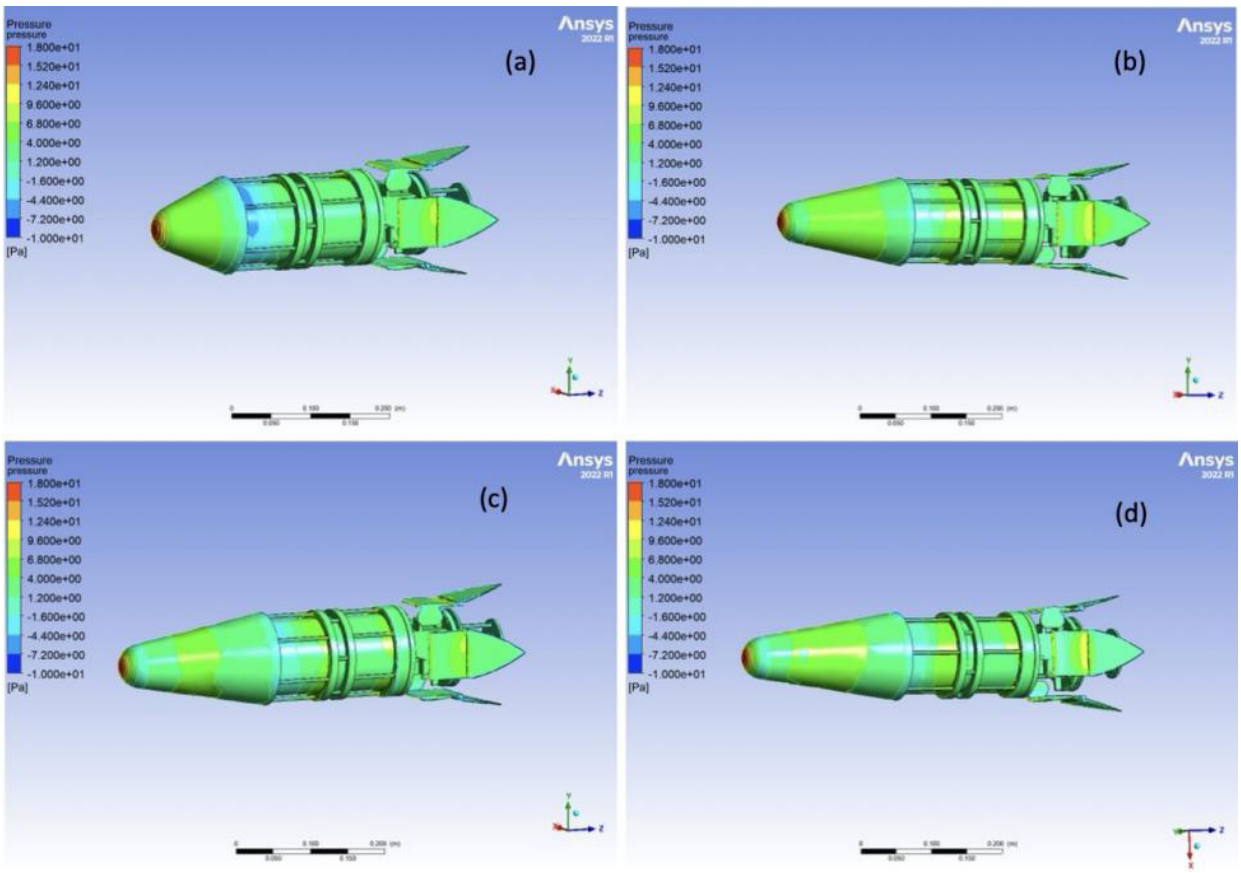

Figure 24: Wall pressure of AUV: (a)Case L1 (b)Case L4 head (c)Case L5 (d)Case L6

All four wall pressures in Figure 24 demonstrate a consistent and uniform trend, represented by the green color. Furthermore, as expected, they all experienced the highest pressure, approximately 18 Pa, at the tip of the head, being the first contact point between the AUV and the fluid. Moving away from the head in a ripple shape, this area of red gradually decreases. At the wings of the AUV, only a small area of yellow is observed, which suggests that the wings contribute a minor percentage to the overall drag experienced during extraction.

Noticeably, from (a) to (d) in Figure 24, the negative pressure region's size decreases, leading to a smaller pressure difference between the front of the AUV and the back of the head. Such a phenomenon results in a less substantial drag force, enhancing the prototype.

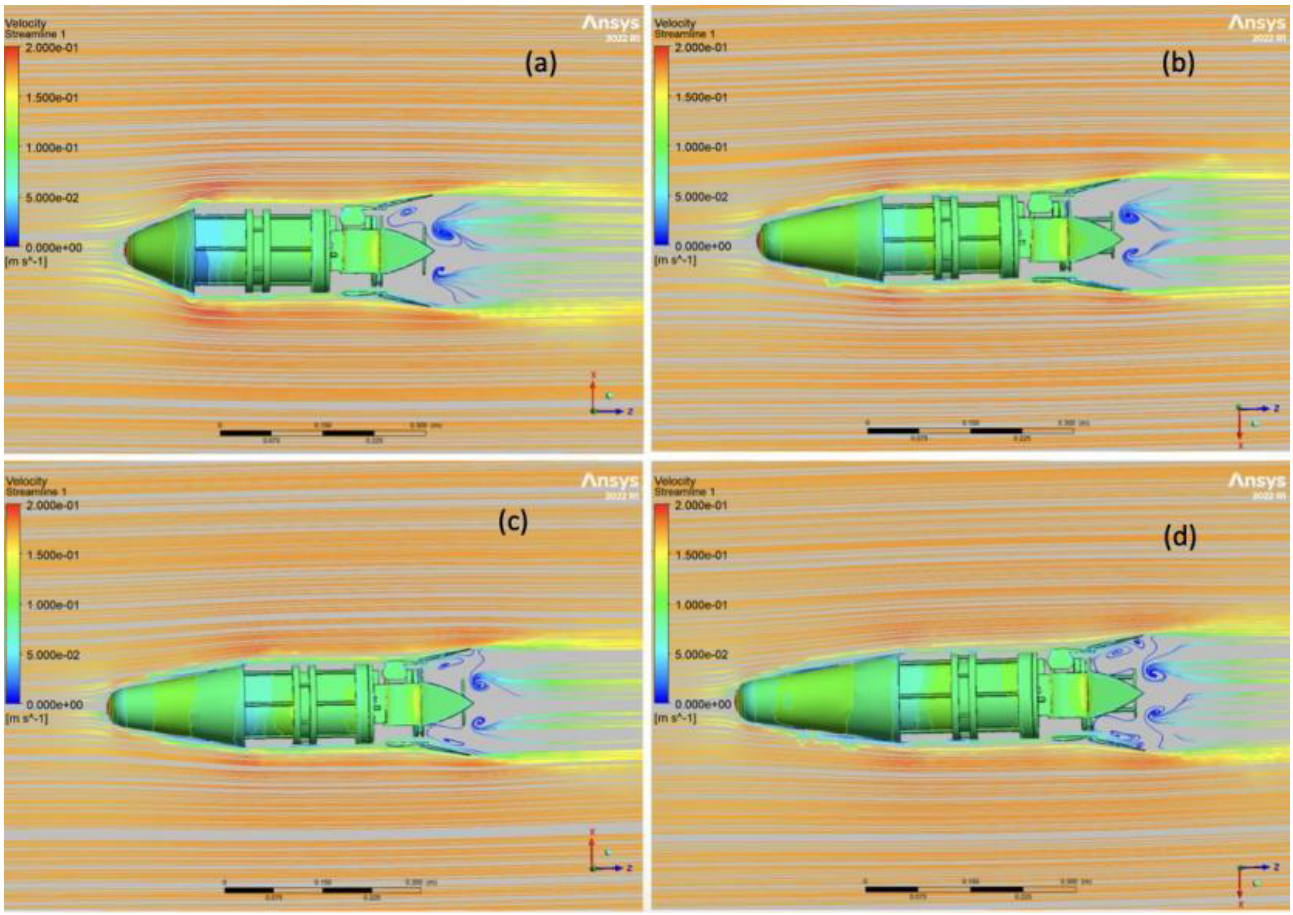

Figure 25: Surface streamline: (a)Case L1 (b)Case L4 (c)Case L5 (d)Case L6

The comparison of the streamline in Figure 25 explains the negative correlation between the length of the head and the experienced pressure drag. As we move from (a) to (d), the turbulence caused by the AUV increases considerably, as indicated by the yellow-colored region near the front of the robot. Referring to Newton's third law of motion, this apparent increase in disturbance is a consequence of a larger pressure acting on the AUV.

Similarly, Case L6 was outperformed by Case L5, despite having a more streamlined shape, as shown in Figure 22, is explained. As the length of the head increases, more viscous force is applied to the robot, given that the surface of the AUV is set to be a no-slip region. However, the decrease in pressure is less evident. This is further supported by the increasing percentage of the viscous drag in the total drag force experienced, as shown in Figure 26.

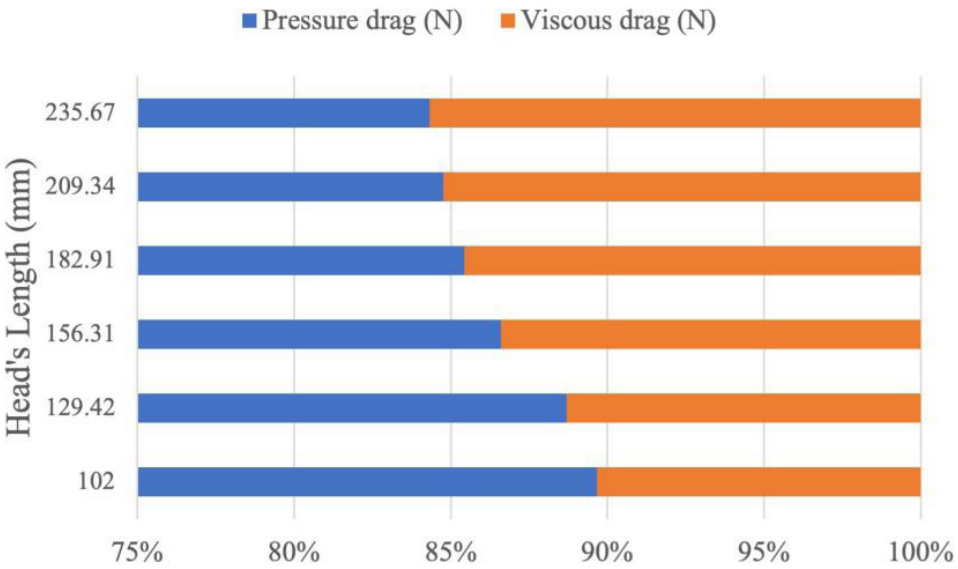

Figure 26: Percent composition of drag forces

All four velocity diagrams in Figure 27 demonstrate a consistent wake region behind the AUV, represented by blue swirling lines. The velocity deficit decays downstream, recovering the free-stream velocity at a downstream distance comparable to the length of the vehicle. Additionally, the front of the AUV exhibits another region of slow fluid velocity, resulting from the AUV pushing back some fluid, thereby reducing some of the momentum of the fluid in front.

Apparently, (a) to (d) in Figure 27 shows a trend in which the areas of redness, representing high-velocity fluids, are decreasing near the end of the head and the rudders. Using the simplified Bernoulli's principle for steady, incompressible, quasi-inviscid flows with streamlines—and disregarding elevation depth—it can be inferred that as the fluid velocity around the AUV increases, the pressure at those locations decreases[14]. The pressure difference between these regions and areas occupied with orange velocity results in a net force pushing the AUV in the direct opposite direction of the flow, contributing to the drag force.

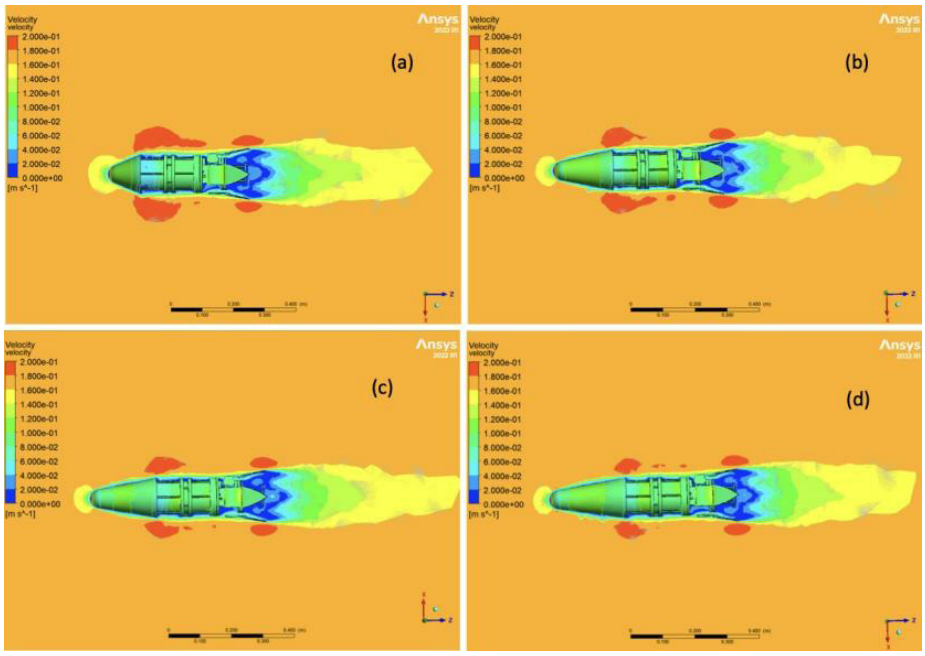

Figure 27: Contour of the velocity magnitude in the plane: (a)Case L1 (b)Case L4 (c)Case L5 (d)Case L6

$$P + \frac{1}{2}\rho v^2 = \text{constant} \quad (15)$$

where P is the pressure at a given point in the fluid; ρ is the density of the fluid; v is the velocity of the fluid at the given point.

In some cases, the faster fluids near the red locations could lead to flow separation, causing the fluids to detach from the AUV's surface, creating a region of low-pressure wake effect immediately after and generating additional drag force.

In conclusion, despite the minimal decrease of 0.0003N in drag force for Case L5, the most optimal design is Case L4. This selection is based on the anticipated smaller turning radius in an aquatic environment, attributable to the force applied on the rudder being situated closer to the AUV's center of mass. This characteristic benefits ecosystems such as coral reefs, where nimble maneuverability and precise navigation are essential.

4.2 Effects of employing a cavity on the hydrodynamics of the AUV

The remaining part of the robot remains consistent with the initial prototype, except for the integration of the 182.91mm long head, which was discovered to be the most optimal in the previous study. As the AUV moves forward, water flows are created around it, generating varying pressure on the wall surface of the AUV due to the no-slip region. Upon examining the previous wall pressure design in Figure 28, it becomes evident that the front and back of the AUV demonstrate a significant 22.4 Pa pressure difference. This pressure differential leads to a suction effect at the rear of the AUV, resulting in a backward pull on the vehicle and generating a force in the opposite direction. Consequently, this increased force contributes to a higher drag force experienced by the AUV during its motion through the water.

The prospect of implementing a cavitation zone was elucidated emerging from this phenomenon. This designated cavity modulates the initial wall pressure encountered at the robot's anterior, directing it towards the extended section, thus instigating water recirculation. This modulation results in diminished wall pressure on the anterior segment. Concurrently, this modification perturbs the flow dynamics, reducing the fluid-head interaction and consequently attenuating viscous drag.

To create the cavity, a connecting cylinder with diameters of 4mm is attached to the front center of the head. Subsequently, at the top of the cylinder, a circle with a diameter of 0.25lb is attached, with a thickness of 1.5mm and lb representing the head's base length. The resultant 3D design is illustrated in Figure 29. During operation, the circular board at the front of the head will experience the highest pressure, resulting in a wake effect region behind it, which will serve as the cavity region.

In this research, the relationship between increasing the cylinder length serves as the connection between the circular board in front and the head concerning the diameter of the circular board. More specifically, the cylinder length was manipulated to be 0.5d, 1d, 1.5d, 2d, and 2.5d, with d representing the diameter of the disk in front of the AUV. From this study, the optimal ratio between the disk's size and the connecting cylinder's length could be determined.

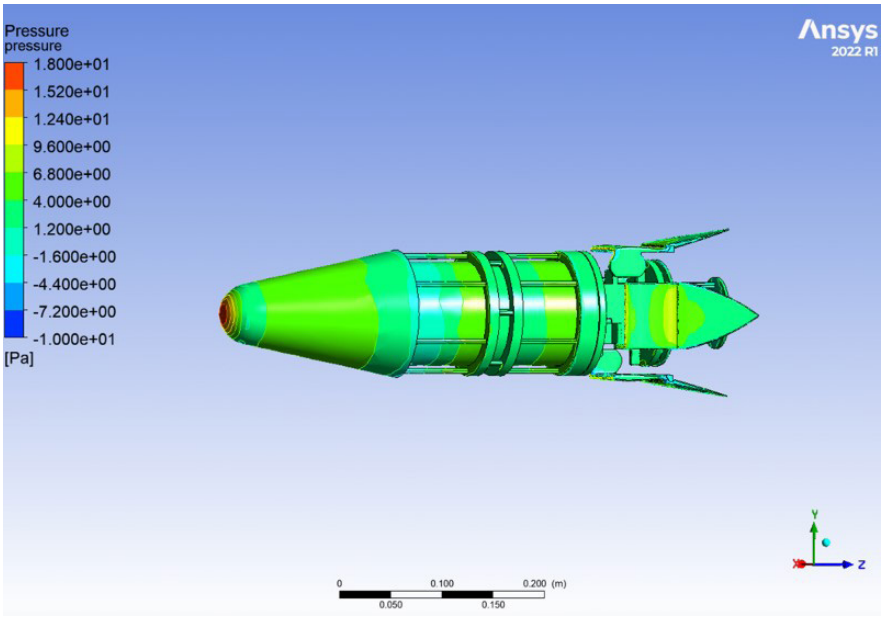

Figure 28: Wall pressure of 182.91mm head length AUV

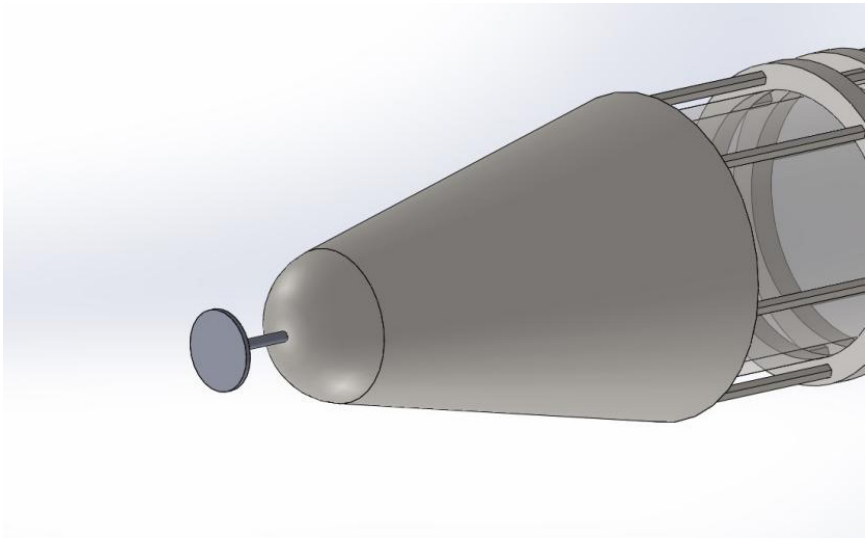

Figure 29: Illustration of a drag reduction disk placed in front of the AUV's head

Table 3: Drag forces of AUV with different connecting cylinder length

	Connecting cylinder's length(mm)	Pressure drag(N)	Pressure drag pct.	Viscous drag(N)	Viscous drag pct.	Total force(N)
Case L1	none	0.0927	85.42%	0.0158	14.58%	0.1085
Case L2	15.625	0.0948	86.54%	0.0148	13.46%	0.1096
Case L3	31.250	0.0937	86.56%	0.0146	13.44%	0.1083
Case L4	46.875	0.0950	86.77%	0.0145	13.23%	0.1095
Case L5	62.500	0.0971	87.07%	0.0144	12.93%	0.1115
Case L6	78.125	0.0983	87.54%	0.0140	12.46%	0.1123

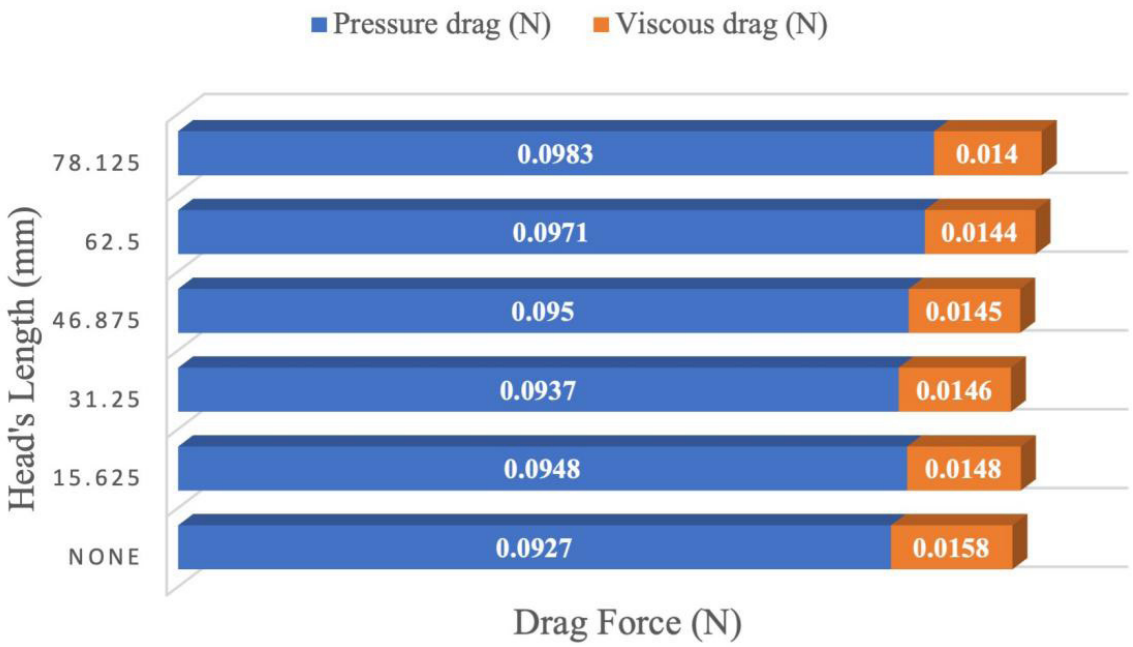

Figure 30: Contributions of drag forces

Figure 30 demonstrates that the lowest drag force is achieved in Case L3, outperforming even the pristine prototype devoid of a disk, thus underscoring the merits of this avant-garde design. As the length of the connecting cylinder augments, there's a reduction in viscous drag, corroborating the postulate that the disk attenuates interactions between the robot's anterior and the incumbent flow. Concomitantly, a decrement in the connecting cylinder's length is paralleled by an upswing in pressure drag force. An exception is noted in Case L3, where a diminution in pressure drag is witnessed, potentially attributed to the mitigation of the suction effect. As this reduced length converges with the remainder, the recirculation zone is displaced further from the anterior, attenuating its efficacy in modulating wall pressure at the robot's forefront, resulting in elevated pressure drag.

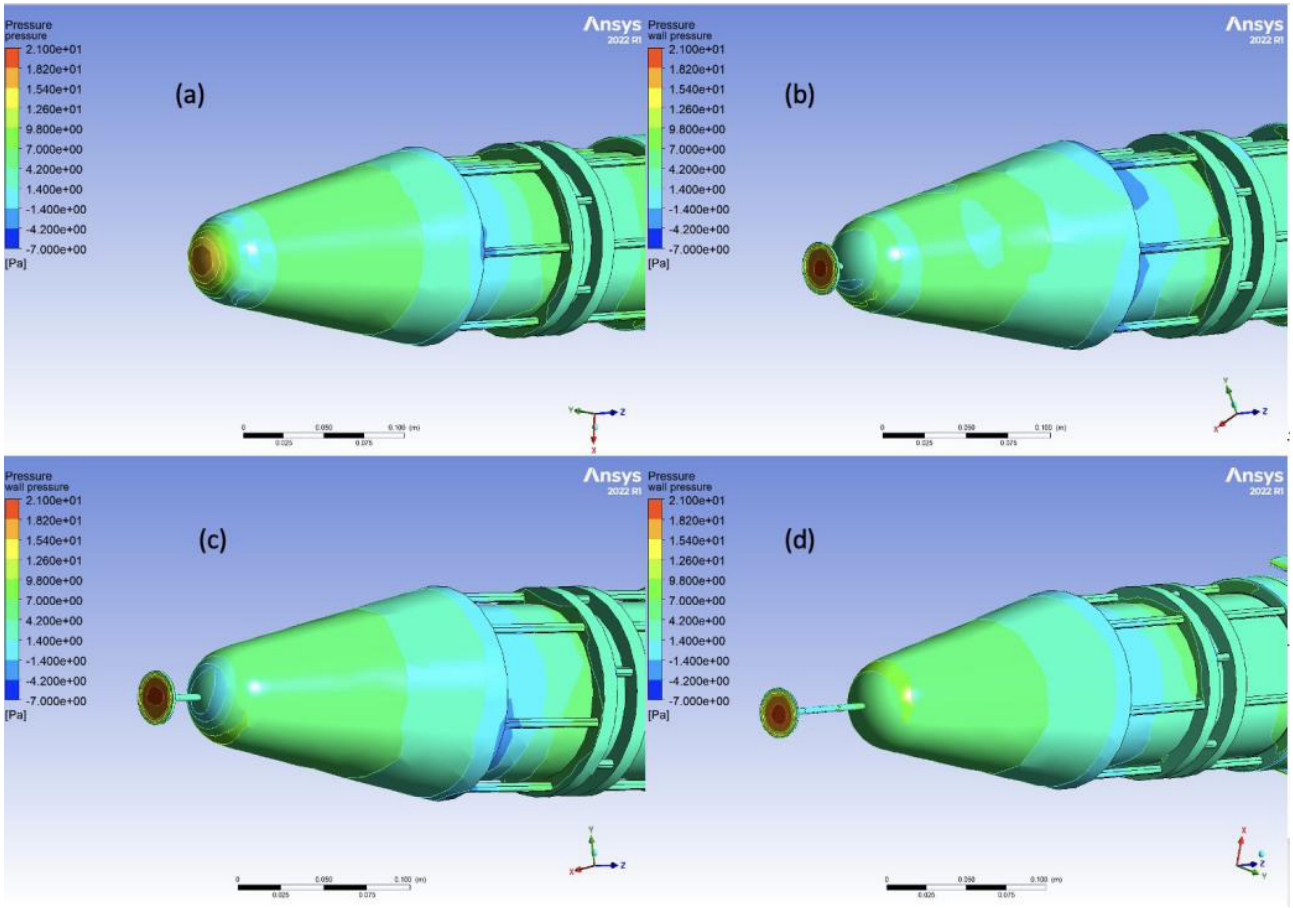

Figure 31: Wall pressure of AUV: (a)Case L1 (b)Case L2 (c)Case L3 (d)Case L6

Across (a) to (d) in Figure 31, the front of the AUV always demonstrates a strong wall pressure since it is the leading part of the robot. However, unlike Figure (a), figures (b) to (d), which share a head extension disk and a connecting cylinder, show an even stronger wall pressure, reaching 21Pa, as opposed to the maximum of 18Pa present in Figure (a). This likely causes the lower pressure drag force observed in Figure (a). This phenomenon is likely due to the circular surface design in Figure (a).

In Figure 31(d), the intended purpose of the head extension was not realized effectively. The presence of recirculation did not successfully reduce the wall pressure experienced by the actual head exterior, as indicated by the universal green color on the head surface. Conversely, figures (b) and (c) demonstrate a significant positive impact on the AUV's head, represented by the sky-blue color. This is likely due to a well-designed head extension and connecting cylinder that promotes smoother flow and reduces flow separation.

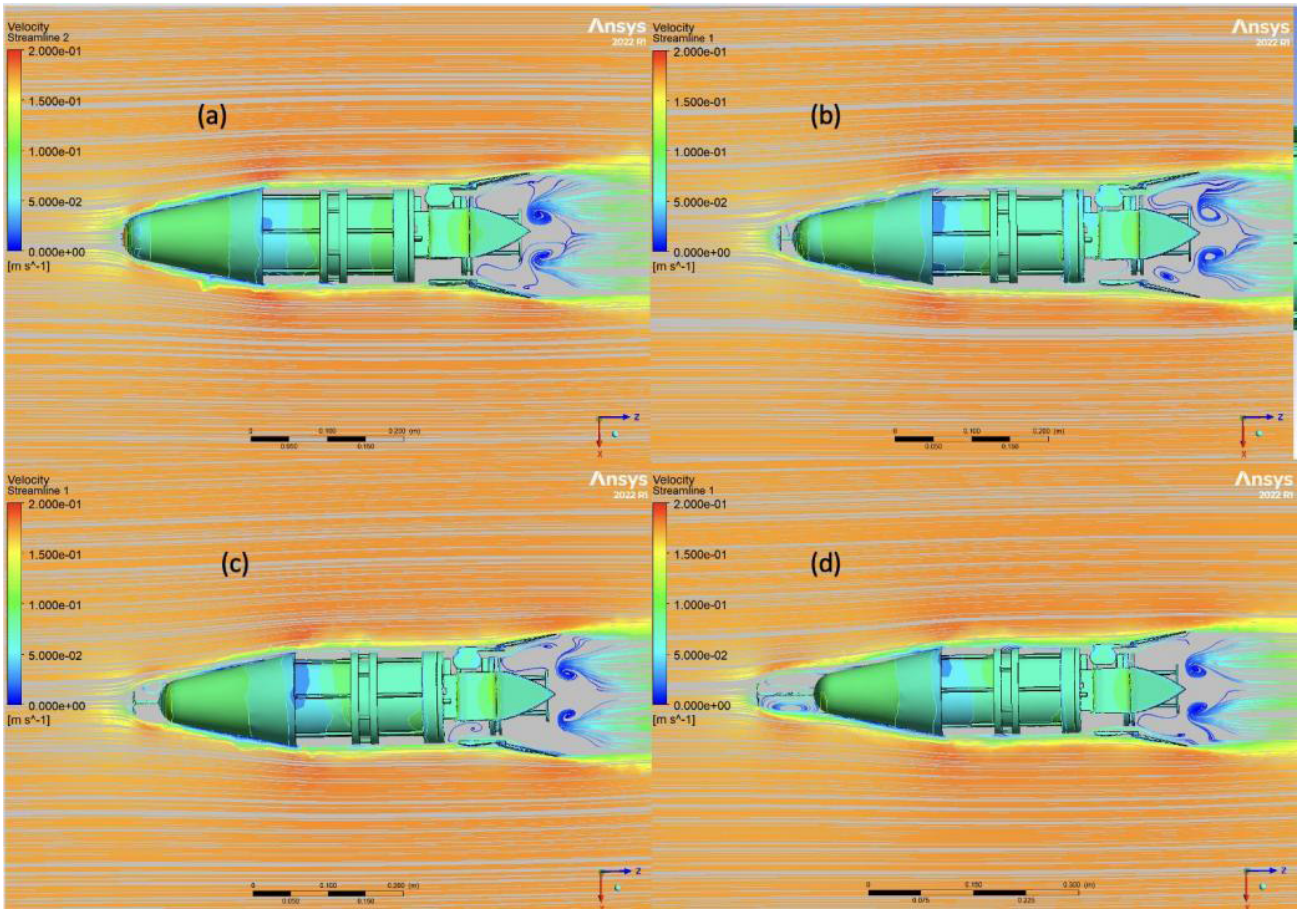

Figure 32: Surface streamline: (a)Case L1 (b)Case L2 (c)Case L3 (d)Case L6

As mentioned above, the recirculation region in Figure (d) did not effectively solve the high pressure on the AUV's head. This phenomenon becomes evident when directly visualizing the flow patterns, as the actual head is located near the downstream end of the recirculation region, as indicated by dark blue colors in Figure 32.

In conclusion, upon integrating a 25mm diameter disk situated 31.25mm proximal to the robot's anterior, a notable diminution in fluid-structure interaction was observed, manifesting in a marked decrement in viscous drag. While the disk introduces certain hydrodynamic anomalies, its critical function is equilibrating the wall pressure gradient across the AUV's anteroposterior axis, mitigating undue suction effects. Consequently, despite the non-laminar flow characteristics induced by the head's geometry, the pressure surge is minimal, overshadowed by the substantial reduction in viscous resistance, culminating in a net decline in total drag of 0.0002N. Although infinitesimal, this difference underlines the effectiveness of the design alteration, verifying the successful output of this investigative study.

5 Experimental Results

In the experimental section, two tests are conducted using the constructed bionic squid-inspired AUV to validate the CFD results and gain insights into the lift forces generated through the manipulation of the rudder, respectively.

First, an experiment is carried out in a freshwater tank to simulate the AUV's operational environment, following a detailed theoretical analysis of the drag forces experienced by the AUV. The experiment's purpose is to measure and document the velocity of the AUV, allowing for a comparison with the predicted drag characteristics.

Second, a specific experiment is designed to investigate the effect of rudder extension on the production of lift forces that can alter the robot's direction and turning radius. This study aims to further optimize the robot's maneuverability. This experimental approach is necessary because CFD simulations may struggle to accurately capture the continuous lift force during complex turning maneuvers, which might induce transient phenomena such as vortex shedding or flow separation. The CFD method's limitations in capturing these dynamics make the experimental investigation a vital step in understanding

the AUV's hydrodynamic behavior comprehensively.

5.1 Velocity Testing

It was necessary to determine the robot's velocity to replicate the water pressure acting on the robot. A water tank measuring 4m in length, 2m in width, and 1m in height was utilized to simulate the ocean environment where the bionic squid AUV was placed. A half-meter ruler stick was positioned inside the water tank to serve as a reference for calculations. Additionally, a stationary camera with a wide field of view was set up to record a substantial duration of the robot's actions. The squid AUV was immersed in the water by utilizing the sink function, which involved allowing water to enter the water tank within the robot. By accumulating the force of gravity, which overcame the force of buoyancy, the AUV began to sink. Subsequently, it was allowed to stabilize within the water tank at a considerable distance from both the surface and the bottom. Upon pushing the joystick to the maximum position on the controller, the water pump operated at its maximum capacity, initiating the robot's movement. A video capturing the robot's movement in water was then uploaded to the Tracker application. A few seconds of operation were selected, during which the acceleration due to the water pump canceled out with the drag force, resulting in a net acceleration of 0. The magnitude of the robot's velocity was extracted using the tools provided by Tracker, as shown in Figure 33. To mitigate inherent uncertainties associated with video analysis, the exported data was further processed using MATLAB to obtain an averaged velocity value, which resulted in 0.175 m/s.

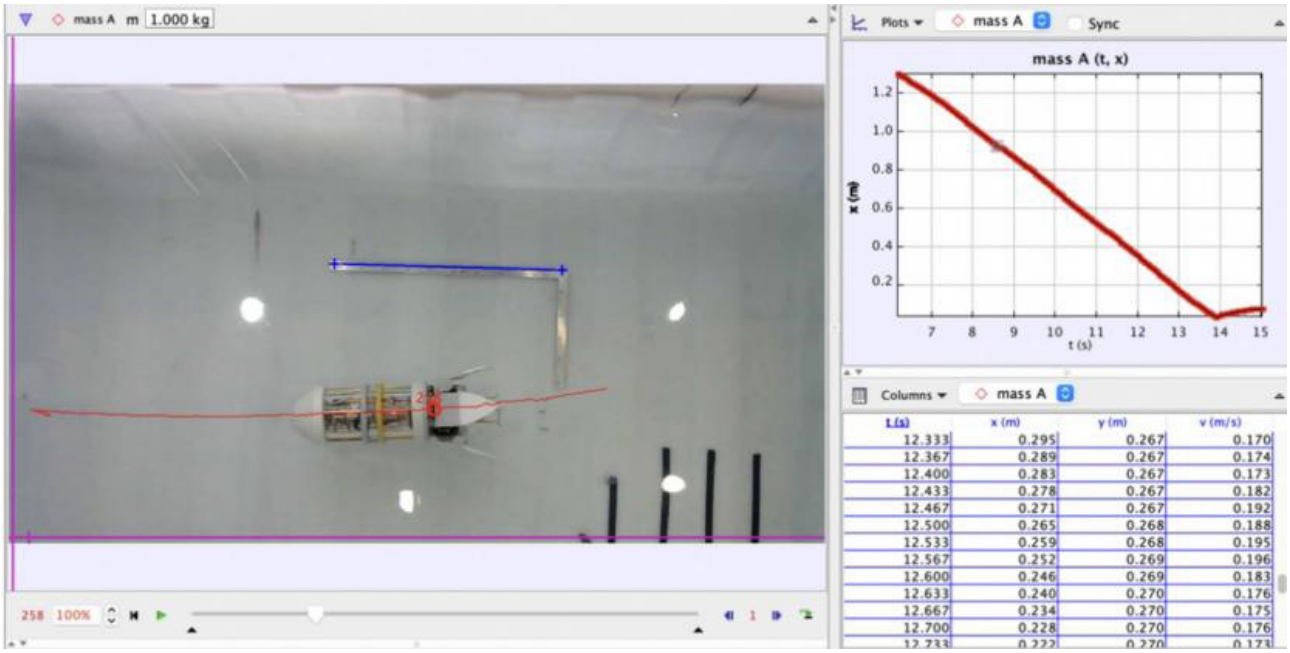

Figure 33: Illustration of the Tracker analysis

Upon further examination, while in motion, the AUV exhibited minimal turbulence in the wake region behind it. This indicates that the incorporation of the head extension has effectively streamlined the overall shape of the AUV, leading to a significant reduction in pressure drag. The AUV's 0.175m/s velocity is suitable for intricate coral reef ecosystems, striking a balance between achieving maximal hydrodynamic efficiency and ensuring the preservation of delicate coral structures.

5.2 The effect of rudder extension angle on the turning radius

Firstly, position the robotic apparatus within an underwater environment devoid of perturbations such as current or wave motion. Allow the robot to submerge and achieve buoyancy equilibrium within this aquatic containment. Manipulate the rudder to a predetermined angle, initially set at 15 degrees, to control the robot's navigation. Next, set the robotic propulsion system to its maximum velocity. Utilize a camera or other suitable recording device to monitor and document the robot's trajectory until it reaches a position perpendicular to its initial navigation path. Subsequently, determine the radius of the robot's navigation path and record this data in the relevant chart or data collection tool. Allow the conditions within the underwater containment to return to a state of rest. Subsequently, repeat the above steps thrice more, altering the rudder's manipulation degree to 25, 35, and

45 degrees for each iteration. This process allows for a comprehensive understanding of how rudder-degree manipulation impacts the navigation trajectory of the robotic apparatus in a confined aquatic environment.

The "Tracker" application analyzes the robot's path and determines the set of points $(xi\,yi)$ the robot traverses on a coordinate plane. To derive the equation of the perpendicular bisector using pairs of points, the application uses the following process:

Let $(x_1 y_1)$ and $(x_2 y_2)$ be two points on the path. The midpoint and gradient of the segment connecting these two points are given by:

$$midpoint: (x_m, y_m) = \left(\frac{x_1 + x_2}{2}, \frac{y_1 + y_2}{2} \right) \tag{16}$$

$$m = \frac{y_1 - y_2}{x_1 - x_2} \tag{17}$$

The gradient of the line perpendicular to this segment is:

$$m_{\perp} = -\frac{1}{m} \tag{18}$$

The equation of the perpendicular bisector is then:

$$y - y_m = m_{\perp} (x - x_m) \tag{19}$$

Subsequent pairs are generated by pairing the i^{th} point with the $(i + \lfloor n/4 \rfloor)^{th}$ point. For finding the intersection of two such bisectors, the equations can be equated:

$$y = m_1 (x - x_{m1}) + y_{m1} \tag{20}$$

$$s_1 (x_o - x_{m1}) + y_{m1} = s_2 (x_o - x_{m2}) + y_{m2} \tag{21}$$

From which, the coordinates of the intersection can be derived:

$$x_o = \frac{s_1 x_{m1} - s_2 x_{m2} + y_{m2} - y_{m1}}{s_1 - s_2} \tag{22}$$

$$y_o = s_1 (x_o - x_{m1}) + y_{m1} \tag{23}$$

Given the property that all points on a circle are equidistant from its center, the turning radius is:

$$radius\,(r) = \sqrt{(x_o - x_1)^2 + (y_o - y_1)^2} \tag{24}$$

The average turning radius from all such derived circles is:

$$r_{\text{average}} = \frac{\sum_{i=1}^{\lfloor \frac{n}{4} \rfloor} r_i}{[n/4]} \tag{25}$$

Finally, for uncertainties, the application uses:

$$if\ \ y = a \pm b\ then\ \Delta y = \Delta a + \Delta b \tag{26}$$

$$if\ \ y = a * b / c\ then\ \frac{\Delta y}{y} = \frac{\Delta a}{a} + \frac{\Delta b}{b} + \frac{\Delta c}{c} \tag{27}$$

Chart 1: Average turning radii for all extensions.

Rudder extension (degree)	Average turning radius (m)	
Case R1	15	2.629
Case R2	25	2.263
Case R3	35	1.959
Case R4	45	1.780

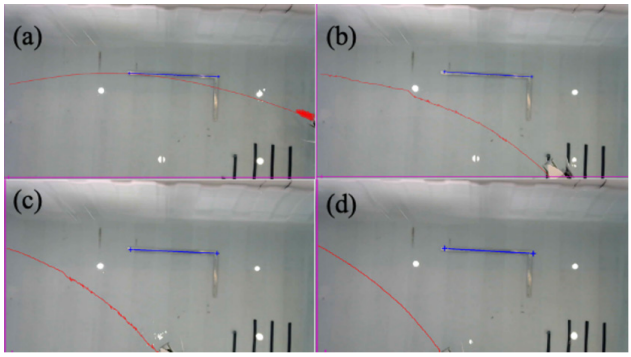

Figure 34: Turning routes for all extensions: (a)Case R1 (b)Case R2 Case R3 (d)Case R4

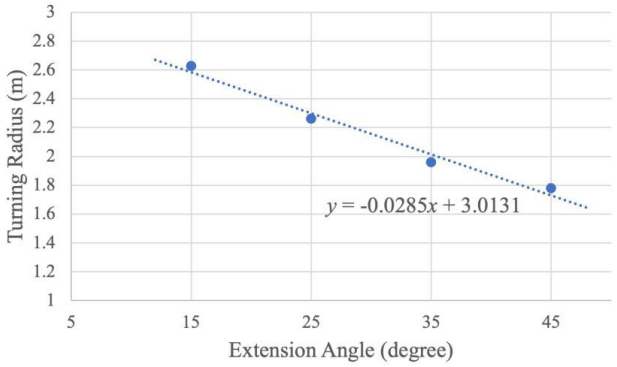

Figure 35: Turning radius plotted against rudder extension angle

Figure 34 and Figure 35 illustrate a clear negative linear correlation between the turning radius and the extension angle. Therefore, to achieve the highest degree of sensitivity when steering, it is imperative to maximize the extension angle.

6 Conclusion

In light of the indispensable role that coral reefs play – both ecologically and economically – understanding and conserving them is paramount. Traditionally, human divers, vulnerable to various physiological complications, were the primary observers in these environments. While designed to address such human vulnerabilities, existing robotic solutions introduced their own challenges, including potential disturbances to marine life. Addressing these gaps, this study presented an optimized AUV inspired by the squid's unique characteristics.

Within the framework of the AUV design, a head length

of precisely 182.91mm was ascertained to be optimal for drag reduction, harmonizing the interplay between viscous and pressure drag induced by its non-slip exterior. By introducing a disk of 25mm diameter, situated 31.25mm proximal to the robot's forefront, the fluid-structure contact is notably reduced, leading to a discernible reduction in viscous drag. Notwithstanding the potential hydrodynamic compromise introduced by the disk, it aids in equalizing the wall pressure gradient spanning from the AUV's anterior to its posterior regions, counteracting undue suction effects. This results in a marginal escalation in pressure drag but yields a net decrement in the overall drag. Experimental observations confirm a propulsion velocity of 0.175m/s for the designated head length and an imperative demand to augment the rudder's deflection angle to achieve optimal turning radius.

The envisioned AUV facilitates the investigation of intricate coral reef ecosystems, serving as an instrumental tool in gathering pivotal data for their conservation. Squid characteristics heavily influence its design. Specifically, its dimensions, resembling a squid, have been meticulously optimized via CFD analyses to achieve drag minimization, thereby enhancing energy efficiency. Further, by emulating the unique locomotive dynamics of squids, potential disturbances to marine flora, such as seagrass, and the broader marine biota are considerably minimized. Additionally, incorporating bionic fins, constructed from pliable materials and fine-tuned through empirical studies, has substantially augmented the AUV's maneuverability capabilities.

By advancing the robotics technology specific to this application, this paper augmented the precision and effectiveness of conservation efforts, thereby ensuring the sustained viability of coral reef ecosystems in the face of anthropogenic challenges such as climatic perturbations and marine pollution.

References

[1] CK-12. 12.1 Fluid Pressure. 2019. URL: https://flexbooks.ck12.org/cbook/ck-12-middle-school-physical-science-flexbook-2.0/section/12.1/primary/lesson/pressure-in-fluids-ms-ps/ (visited on 07/07/2019).

[2] Gautham Anne. The Physics of Water Wakes. 2021. url: https://sites.imsa.edu/hadron/2021/11/ 07/the-physics-of-water-wakes/ (visited on 11/07/2021).

[3] T. R. Auton. "The lift force on a spherical body in a rotational flow." In: Journal of Fluid Mechanics 183 (1987), pp. 199–218. doi: 10.1017/S002211208700260X.

[4] William S. Burdic and James F. Bartram. "Underwater Acoustic System Analysis by William S. Burdic". In: The Journal of the Acoustical Society of America 76.3 (Sept. 1984), pp. 996– 996. ISSN: 0001-4966. doi: 10.1121/1.391242. eprint: https://pubs.aip.org/asa/jasa/article pdf/76/3/996/11949459/996_1_online.pdf. url: https://doi.org/10.1121/1.391242.

[5] Richard Flay. "Bluff Body Aerodynamics". In: Apr. 2013, pp. 59–84. isbn: 978-4-431-54336-7. doi: 10.1007/978-4-431-54337-4_3.

[6] Terry P Hughes, JT Kerry, and T Simpson. Large-scale bleaching of corals on the Great Barrier Reef. 2018.

[7] Kekuewa Kikiloi et al. "Papaha¯naumokua¯kea: Integrating Culture in the Design and Management of one of the World's Largest Marine Protected Areas". In: Coastal Management 45.6 (2017), pp. 436– 451. doi: 10.1080/08920753.2017.1373450. eprint: https://doi.org/10.1080/08920753.2017.1373450. url: https://doi.org/10.1080/08920753.2017.1373450.

[8] Diana Li. Locomotion. url: https://gillylab.stanford.edu/locomotion2.

[9] MakerFocus. MakerFocus ESP32 Development Board SX1262 863 928MHz LoRaWAN WiFi Bluetooth Dual Core 240MHz Integrated CP2102 with 0.96" OLED Display and Antenna for Ar duino NodeMCU Intelligent Scenes. 2017. url: https://www.amazon.com/MakerFocus-DevelopmentBluetooth-0-96inch-Display/dp/B076MSLFC9 (visited on 10/21/2017).

[10] F. Menter. "Zonal Two Equation k-w Turbulence Models For Aerodynamic Flows." In: 23rd Fluid Dynamics, Plasmadynamics, and Lasers Conference. doi: 10.2514/6.1993-2906. eprint: https://arc.aiaa.org/doi/pdf/10.2514/6.1993-2906. url: https://arc.aiaa.org/doi/abs/10.2514/6.19932906.

[11] F. R. Menter. "Two-equation eddy-viscosity turbulence models for engineering applications." In: AIAA Journal 32.8 (1994), pp. 1598–1605. doi: 10.2514/3.12149. eprint: https://doi.org/10.2514/3. 12149. url: https://doi.org/10.2514/3.12149.

[12] Peter J Mumby and Robert S Steneck. "Coral reef management and conservation in light of rapidly evolving ecological paradigms." In: Trends in ecology & evolution 23.10 (2008), pp. 555–563.

[13] NOAA. Coral reef ecosystems. 2019. url: https://www.noaa.gov/education/resource-collections/ marine-life/coral-reef-ecosystems#:~:text=Benefits%20of%20coral%20reef%20ecosystems,food% 2C%20income%2C%20and%20protection (visited on 02/01/2019).

[14] Agamenon R. E. Oliveira. "History of the Bernoulli Principle". In: Advances in Mechanism and Machine Science. Ed. by Tadeusz Uhl. Cham: Springer International Publishing, 2019, pp. 1161–1178. isbn: 978-3-030-20131-9.

[15] NR Olsen. CFD algorithms for hydraulic engineering. 2000.

[16] Tibi Puiu. "Coral reefs generate 36billionintourismeveryyearbutweofferlittleinreturn" in: (2017).

[17] Steven Vogel. "Flow-assisted mantle cavity refilling in jetting squid." In: The Biological Bulletin 172.1 (1987), pp. 61–68.

[18] Wikipedia. Squid. url: https://en.wikipedia.org/wiki/Squid.

[19] M. H. Zawawi et al. “A review: Fundamentals of computational fluid dynamics (CFD)”. In: AIP Conference Proceedings 2030.1 (Nov. 2018), p. 020252. ISSN: 0094-243X. doi: 10.1063/1.5066893. eprint: https://pubs.aip.org/aip/acp/article-pdf/doi/10.1063/1.5066893/7654457/020252_1\ _online.pdf. url: https://doi.org/10.1063/1.5066893.

Appendices

A Program Logic

A.1 Onshore

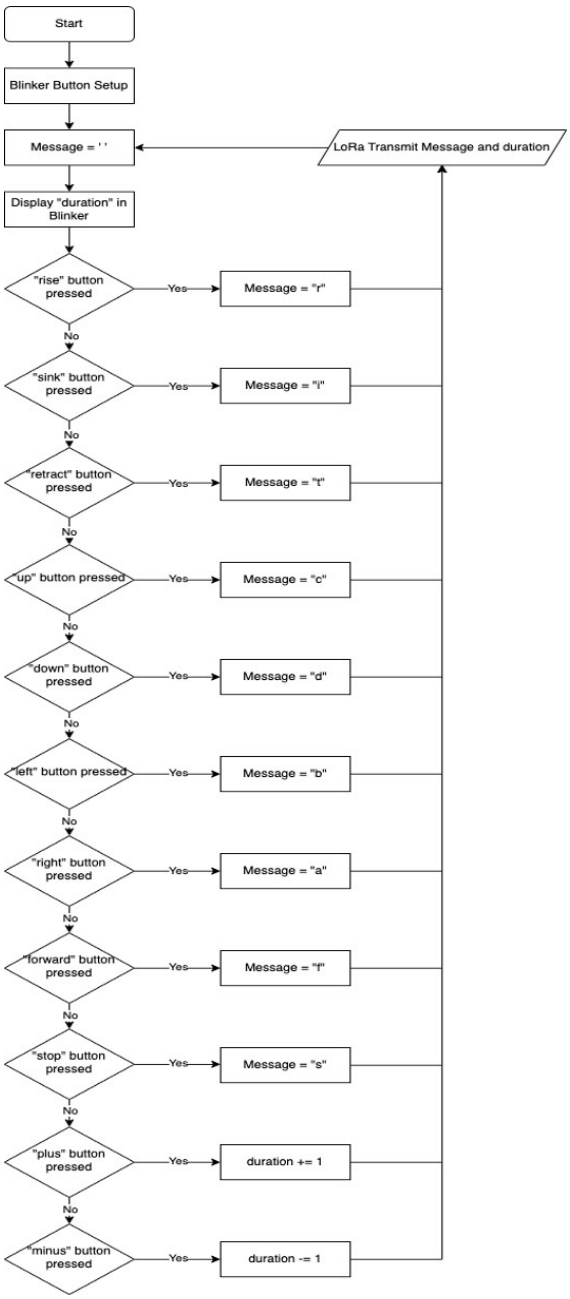

Figure 36: Onshore program logic diagram

A.2 AUV

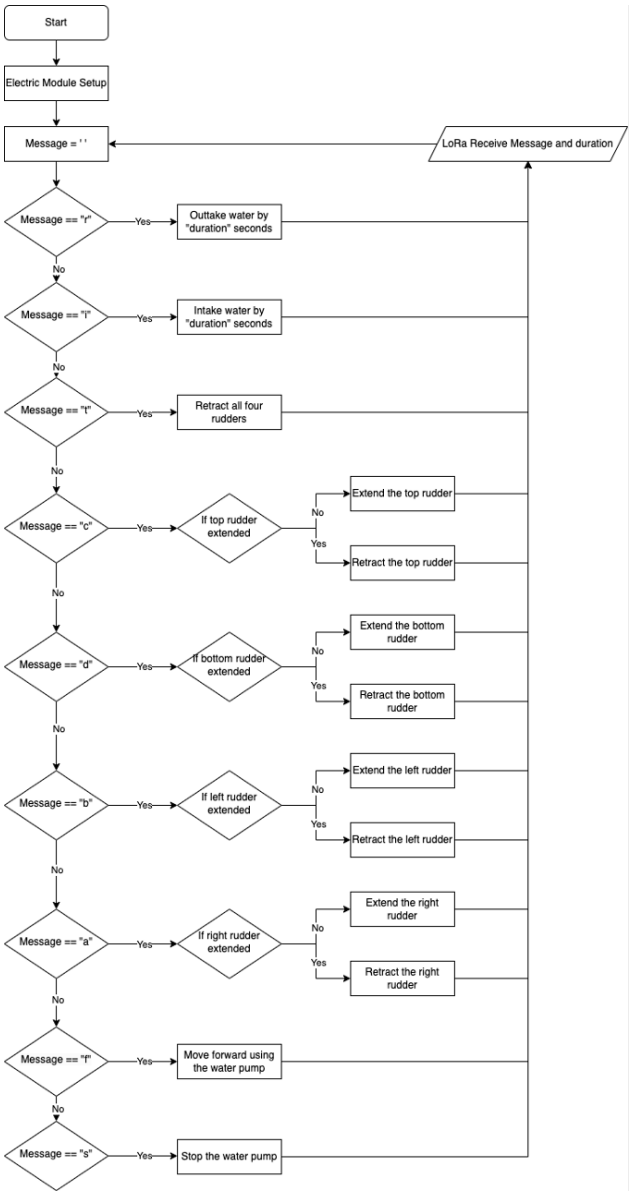

Figure 37: AUV program logic diagram

Acknowledgment

First and foremost, I would like to extend my deepest appreciation to Mr. Pimental. His role was not just that of a supervisor but also of a mentor who guided me throughout this project. Whenever I encountered a roadblock or felt uncertain, he was there with sage advice, reassuring me and providing clarity. His profound knowledge and passion for hydrodynamics were infectious, leading me to cultivate a newfound love for the intricacies of hydrodynamics analysis and the nuances of optimizing design. Under his tutelage, I understood the deeper layers of the subject matter and the intricate webs

of its applications.

Furthermore, Dr. Yang offered tremendous moral support whenever my results were unsatisfactory or when the road seemed rough. He emphasized the importance of perseverance and learning from our mistakes. This constant encouragement from him drove me to push forward, even during those moments when giving up seemed like the easier option.

Lastly, I owe a massive debt of gratitude to my parents. Their unwavering belief in my abilities and generous financial support were the backbones of my endeavor. The resources they provided, both in terms of high-performing laptops, which became the bedrock for my CFD and CAD operations, and the state-of-the-art electronics and 3D printing facilities, were invaluable to the success of my project. These tools allowed me to breathe life into my designs and see them come to fruition. More than just the physical resources, their emotional and moral support played an instrumental role. They stood by me through the highs and lows, always ready to offer encouragement or lend a listening ear.

They reminded me of the bigger picture and the importance of my journey, not just the destination.

In conclusion, it's often said that behind every successful individual is a team of supportive people. In my case, Mr. Pimental, Dr. Yang, and my parents have been that unwavering support force. Their faith in me and the resources they've provided have been instrumental in shaping my project and my growth as an individual in this field.